Peri-Tethyan water column deoxygenation and euxinia at the Paleocene Eocene Thermal Maximum

L. Behrooz[1], B.D.A. Naafs[1], K.W.R. Taylor[1,#], F.M. Monteiro[2], A.J. Dickson[3], A. Pearson[4] and R.D. Pancost[1]*

[1] Organic Geochemistry Unit, School of Chemistry, School of Earth Sciences, Cabot Institute for the Environment, University of Bristol, UK

[2] BRIDGE, School of Geographical Sciences, University of Bristol, UK

[3] Centre of Climate, Ocean and Atmosphere, Department of Earth Sciences, Royal Holloway University of London, UK

[4] Department of Earth and Planetary Sciences, Harvard University, USA

*Corresponding author: R.D.Pancost@bristol.ac.uk

[#] Present address: Elementar North America

Key Points:

- Photic zone euxinia occurred in the Peri-Tethys during the PETM.
- Photic zone euxinia was more likely stimulated by an increase in the nutrient inventory rather than as a direct response to warming.
- The restriction of photic zone euxinia to specific regions is governed by geography

Abstract

The Paleocene–Eocene Thermal Maximum (PETM) is associated with climatic change and biological turnover. It shares features with the Oceanic Anoxic Events (OAEs) of the Mesozoic, such as transient global warming and biogeochemical perturbations. However, the PETM experienced a more muted expansion of marine anoxia compared to the Mesozoic OAEs (especially OAE 2), with benthic deoxygenation being geographically restricted and limited evidence for photic zone euxinia. We explore the extent and drivers of marine deoxygenation during the PETM using biomarkers for water column euxinia and anoxia and data-constrained biogeochemical climate model (cGENIE) simulations. These reveal that the water column in the North-East Peri-Tethys became anoxic during the PETM, with euxinic conditions reaching the photic zone. Our simulations show that this developed

due to a global increase in the ocean nutrient inventory, similar to findings for OAE 2. The particularly strong regional response in the NE Peri-Tethys appears to arise from a combination of global forcing and regionally restricted circulation. Unlike OAE 2, anoxia and PZE do not become widespread in our PETM simulations, consistent with geochemical and biological indicators. This globally muted response could result from a reduced oceanic phosphate inventory prior to the PETM and/or a smaller increase during it relative to the mid-Cretaceous ocean. Our observations suggest that similar feedback mechanisms operated in response to disparate Cenozoic (PETM) and Mesozoic (OAEs) transient global warming events, while also highlighting that background conditions such as geography and nutrient status are crucial in modulating the sensitivity of Earth's system to them.

Summary: Ancient global warming events can help us understand the impact(s) of current global warming. A response to many past global warming events has been the expansion of oxygen deficient waters in the ocean. This is also true for the Paleocene-Eocene Thermal Maximum that occurred about 56 million years ago. Here we show that this decrease in oxygen was so dramatic in the Peri-Tethys (a precursor to the Mediterranean Sea of today) that it extended into the photic zone and stimulated the growth of unusual bacteria that require both light and hydrogen sulfide. This did not appear to be a direct result of warming but rather an indirect result – warming caused the delivery of nutrients that stimulated the production of organic matter, which consumed oxygen in the underlying waters when it sank and degraded.This has potential analogues throughout Earth history and potentially for the future, but our work also shows that the magnitude of this response will be governed by other factors, such as the restriction of circulation and location of upwelling zones.

1. Introduction

The Paleocene–Eocene Thermal Maximum (PETM) (Kennett and Stott, 1991) at ~56 Ma is the largest and most abrupt transient global warming event (hyperthermal) of the Cenozoic and lasted for ~120–220 ka (Westerhold et al., 2018). The PETM is characterized by a negative stable carbon isotope ($\delta^{13}C$) excursion (CIE) and abrupt increase in global temperature (4 to 8˚C in <10 ka (Sluijs et al., 2006; Zachos et al., 2006; Dunkley Jones et al., 2010; Inglis et al., 2020)). The negative CIE documents the rapid release of ^{13}C-depleted carbon into the ocean-atmosphere system, although its source remains contested (Dickens et al., 1997; Svensen et al., 2004; Zeebe et al., 2009; Gutjahr et al., 2017; Babila et al., 2022). In addition to warming, the PETM is associated with changes in the hydrological

cycle, terrestrial sediment flux, nutrient input to the ocean, black shale deposition in some basins, and increased algal productivity (Carmichael et al., 2017 and references therein).

Many of these features are similar to those proposed for the Oceanic Anoxic Events (OAEs) of the Mesozoic (Schlanger et al., 1976; Jenkyns, 2010; Monteiro et al., 2012). OAEs (Robinson et al., 2017) exhibit rather profound differences in the magnitude and geographical extent of deoxygenation, including the deposition of organic-rich sediments (Trabucho-Alexandre et al., 2012). For example, photic zone euxinia (PZE) has been inferred for several OAEs from the occurrence of isorenieratane, a derivative of the carotenoid isorenieratene that is produced by green sulfur bacteria (GSB; Chlorobiaceae), photoautotrophs that obligately require H_2S as a reductant (Overmann et al., 2008, and references therein) and are therefore diagnostic for PZE (Koopmans et al., 1996). Isorenieratane and other GSB pigments are remarkably widespread in Tethyan and Atlantic Ocean sediments deposited during Cenomanian-Turonian OAE 2 (94 Ma), including in deep sea settings (Sinninghe Damsté et al., 1998; Kuypers et al., 2002; Pancost et al., 2004), whereas the occurrence of these biomarkers during the end-Aptian OAE 1a appears to be relatively restricted (Naafs and Pancost, 2014). Similarly, OAE 2 is associated with a positive carbon isotope excursion, directly recording the burial of ^{13}C-depleted organic matter (Arthur et al., 1987), whereas other OAEs exhibit more complex carbon isotope stratigraphy, indicating complex interactions between carbon release and burial (Jenkyns et al., 2010).

Given the complexity of Mesozoic OAEs and fewer preserved sedimentary records, it is inappropriate to draw universal similarities and contrasts between them and the PETM. However, the PETM does markedly differ from the well-studied OAE 2. Although marginal marine sites record a decrease in ocean oxygenation during the PETM (Dickson et al., 2014b, 2014a; Sluijs et al., 2014; Papadomanolaki et al., 2022), the open ocean appears to have experienced only minor seafloor deoxygenation (Winguth et al., 2012; Zhou et al., 2016; Clarkson et al., 2021), with limited deposition of organic-rich sediments (Papadomanolaki et al., 2022 and references therein). Six PETM sites contain biomarker evidence (isorenieratane) for photic zone euxinia (PZE) and all are marginal sites or restricted basins, including the Arctic Ocean (IODP Site M0004; Sluijs et al., 2006); North Sea (Fur and Store Bælt; Schoon et al., 2015), West Siberian Sea (well 10; Frieling et al., 2014), Gulf Coastal Plain (Harrell Core; Sluijs et al., 2014), eastern shelf of the South Atlantic (Dahomey Basin; Frieling et al., 2017), and in the Peri-Tethys (Kurpai; Gavrilov et al., 2003). However, apart from the enclosed and hydrographically restricted Arctic Ocean, isorenieratene derivatives have not been found in PETM deep water settings. Where found in shelf settings their concentrations are lower than in many OAE 2 sections, and their occurrence is less persistent stratigraphically. Therefore, despite similar evidence of

warming and other (biogeochemical) feedback mechanisms, the PETM experienced a much more limited degree of ocean deoxygenation and especially PZE compared to OAE 2. The reasons for this reduced response are poorly understood (Papadomanolaki et al., 2022). Here we investigate the mechanisms that drove marine deoxygenation during the PETM by *i*) providing new biomarker data for the spread of anoxia and PZE from marine sites in the Peri-Tethyan region and *ii*) constraining an Earth system model of intermediate complexity (EMIC) with those new observations.

To reconstruct the spread of ocean water column anoxia and photic zone euxinia (PZE) across the PETM and supplement observations from previous studies, we analysed sediments from three Peri-Tethyan Basins, semi-restricted basins that could have been particularly vulnerable to marine deoxygenation (Guru-Fatima, Kheu River, and Dzhengutay), and one open margin setting from the North-West Atlantic; Zumaia (Fig. 1). The occurrence of the PETM throughout the NE Peri-Tethys marginal settings is associated with the deposition of organic-rich sediments (Dickson et al., 2014b; Gavrilov et al., 2003), especially at the onset of the CIE (Shcherbinina et al., 2016). Collectively, these sections allow Paleocene-Eocene organic rich shales to be traced across about 2500 km, from Central Asia to the Caucasus (Gavrilov et al., 2003; Gavrilov et al., 2009), including the Guru-Fatima section located in the eastern (Central Asia) region and the Dzhengutay and Kheu River sections located in the western (Caucasus) regions (Figure 1). The Zumaia section is located in the North-West Atlantic and deposited in lower to mid bathyal settings, at about 1 km depth (Rodríguez-Tovar et al., 2011). It is the most complete and representative section of the early Paleogene of the Pyrenees (Pujalte et al., 1998). All four sites contain the PETM as indicated by the characteristic negative $\delta^{13}C$ CIE as well as characteristic biotic signatures (see methods).

We used molecular fossils (biomarkers) to reconstruct water column anoxia and PZE at these four locations. Specifically, we used the ratio of lycopane relative to the C_{31} *n*-alkane as an indicator for water column dysoxia/anoxia (Sinninghe Damsté et al., 2003) and the occurrence of isorenieratane (and its derivatives) as an indicator for PZE (Koopmans et al., 1996). The differences in thermal maturity and sedimentation rate between the sites, as well as the different sampling resolution, make it difficult to compare absolute biomarker concentrations and we therefore focus on temporal trends within each section. We also report wider biomarker/geochemical data for these sections to provide additional environmental and climatic context. This includes TEX_{86}-based sea surface temperatures (SSTs; Schouten et al., 2002) compound specific $\delta^{13}C$ values of pristane and phytane to trace changes in carbon cycling, and bulk $\delta^{15}N$ values to constrain changes in the marine nitrogen cycle. These observations are then compared to the available literature data for

PZE (Sluijs et al., 2006; Schoon et al., 2015; Frieling et al., 2014; Sluijs et al., 2014; Frieling et al., 2017; Gavrilov et al., 2003) as well as wider literature on global marine deoxygenation (compiled by Papadomanolaki et al., 2022) and interpreted in the context of the EMIC model cGENIE to infer global changes in marine deoxygenation and euxinia across the PETM ocean and investigate the mechanisms that drove those changes. For the cGENIE simulations we use the model set-up as detailed in Remmelzwaal et al. (2019) and compare these with previously published data-constrained simulations from OAE 2 (Monteiro et al., 2012; Naafs et al., 2019).

2. Materials and Methods

2.1. Sample material

The Kheu River (KR) section is comprised of organic lean silty claystones (<1 wt.% TOC) with an intermediate organic rich shale (mean 5 wt.%) (Dickson et al., 2014b). Elemental sulfur values also increase from <1 wt.% in the organic lean sections to ~4 wt.% in the organic rich horizon. A bulk $\delta^{13}C_{org}$ excursion of –4.5 ‰ is expressed in the section, with values decreasing from around –26 ‰ in the organic lean sediments to –30.5 ‰ in the organic rich horizon, representing the PETM (Dickson et al., 2014). Kheu River sediments were obtained from an outcrop exposure that had been cut back to avoid exposed materials and are the same as reported in Dickson et al. (2014).

The Guru-Fatima section is comprised of grey calcareous mudstone (<1 wt.% TOC), overlain by an organic rich shale horizon (7–20 wt.% TOC), which is covered by a laminated mudstone (~3 wt.% TOC) and an organic lean mudstone (<1 wt.% TOC; Dickson et al., 2014). Elemental sulfur varies from <1 wt.% in the deepest and top horizons to 3 wt.% in the organic rich horizon (**Error! Reference source not found.**). The PETM is characterized by a bulk $\delta^{13}C_{org}$ CIE of –4 ‰ in the section, with values of –26 ‰ in the deepest horizon (grey calcareous marls), –30 ‰ in the organic rich shale and –28 ‰ in the overlying laminated mudstone (Dickson et al., 2014). Guru-Fatima sediments were sampled from an archived drill core at the Geological Institute of the Russian Academy of Science.

The Dzhengutay section is comprised of calcareous mudstone (<1 wt.% TOC) with an intermediate organic rich shale horizon (~3.5 wt.% TOC) (Dickson et al., 2014b). The elemental sulfur content increases from non-detectable values in the calcareous mudstone to ~1 wt.% in the organic rich horizons. The PETM is reflected in a bulk $\delta^{13}C_{org}$ excursion of –4 ‰, with values of about –26 ‰ in the calcareous mudstone and about –29 ‰ in the intermediate organic rich shale (Dickson et al., 2014b). Dzhengutay sediments were

sampled from an outcrop exposure that had been cut back significantly to prevent potentially degraded and contaminated surface sediments from impacting biomarker analyses.

In addition to the northern Peri-Tethys sections, we analysed the Zumaia section (re-sampled from the same core that was studied in Manners et al., 2013), located in the western Peri-Tethys. Zumaia is deposited in lower to mid bathyal settings, at about 1 km depth (Rodríguez-Tovar et al., 2011) and is the most complete and representative section of the early Paleogene of the Pyrenees and represents a suitable open marine section for examining the Paleocene–Eocene boundary (Pujalte et al., 1998; Dunkley Jones et al., 2018; Duller et al., 2019). The PETM is identified based on the 3.7‰ carbon isotope excursion as recorded by bulk organic matter as described in Manners et al. (2013).

Biomarker analyses were conducted on a total of 33 newly extracted samples, comprising 13 samples from Dzhengutay, 10 samples from Guru Fatima, and 10 samples from Zumaia. Biomarkers in Kheu River samples were previously extracted (Dickson et al., 2014b) and are the same as those reported in that study; here we present new data on the abundance of isorenieratene and its derivatives. Prior to any treatment, rock samples were washed (by methanol and dichloromethane (DCM) to remove any potential surface contamination), and then the samples were powdered using a solvent-cleaned ball mill.

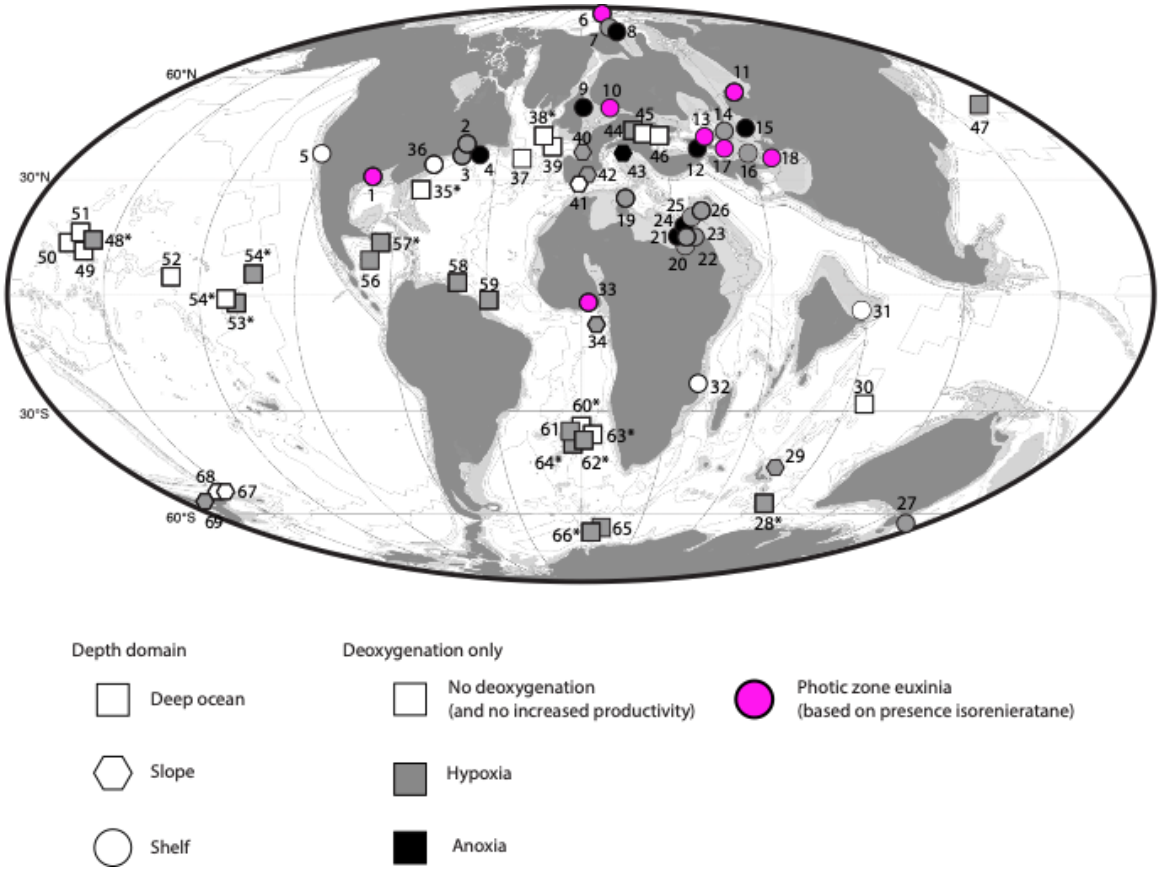

Figure 1. *Paleocene-Eocene world map (adapted from Papadomanolaki et al., 2022, with permission and assistance) highlighting redox indicators for the main body of the PETM. Numbers refer to site names from Papadomanolaki et al (2022). Purple symbols indicate sites with evidence for anoxia but also PZE, based on either our study or previous work: 1) Gulf Coastal Plain (Harrell Core; Sluijs et al., 2014); 6) Arctic Ocean (IODP Site M0004; Sluijs et al., 2006); 10) North Sea (Store Baelt; Schoon et al., 2015); 11) West Siberian Sea (Well 10; Frieling et al., 2014); 13) North Central Peri-Tethys (Kurpai and Guru Fatima; Gavrilov et al., 2003 and this paper); 17/18) North East Per-Tethys (Kheu River and Dzhengutay; this paper); 33) Eastern Shelf of the South Atlantic (Dahomey Basin, Frieling et al., 2017).*

2.2. Biomarker extraction

The methods for Kheu River biomarker extraction, separation and analysis are explained elsewhere (Dickson et al., 2014b). To obtain total lipid extracts (TLEs) from the other sites, about 5 g of (Dzhengutay and Guru Fatima) sediment were microwave solvent extracted ((MILESTONIE Ethos Ex) with 10 ml of a mixture of dichloromethane (DCM) and methanol (MeOH) (1:1, vol). The microwave program comprised a 10 min ramp to 70 °C (max. 1000 W), followed by a 10 min hold at 70 °C (max. 1000 W) and 20 min cooling period. After microwave extraction the samples were centrifuged (1500 rpm, 5 minutes) and the resulting supernatant collected. An additional 10 ml of DCM:MeOH were added to the sediment, centrifuged, and the supernatant again collected. This procedure was repeated four times. To obtain TLEs from the organic lean Zumaia sediments, 35 g of sediment were extracted with 220 ml of DCM:MeOH (1:1, vol) azeotrope using a Soxhlet apparatus for 24 hrs. Solvent-washed activated copper turnings were added to the TLE for 24 hrs to remove elemental sulfur. The TLE was then concentrated using rotatory evaporator.

TLEs were separated into three fractions (aliphatic, aromatic and polar) using short (4 cm) silica gel open column chromatography. Aliphatic, aromatic, and polar fractions were eluted using 3 ml of hexane, 4 ml of hexane:DCM (3:1), and 4 ml of DCM:MeOH (1:2), respectively. The Zumaia TLEs (similar to those from Kheu River (Dickson et al., 2014b)) were separated into a fatty acid and neutral fractions via silica gel flash column chromatography using 7 ml of chloroform and 7 ml of chloroform:acetic acid (100:1), respectively. The neutral fraction was further separated into two fractions (apolar and polar) on an alumina column using 5 ml of *n*-hexane:DCM (9:1) and 4 ml DCM:MeOH (1:2), respectively. The apolar fractions were used for GC-MS analysis. For all samples, prior to GC-MS analysis, a known amount of C_{36} *n*-alkane was added as an internal standard for the

(semi-)quantification of the biomarkers of interest (e.g., isorenieratane). To analyse the distribution of glycerol dialkyl glycerol tetraether (GDGTs) and quantify the TEX_{86}-SST proxy (Schouten et al., 2002) the polar fractions or TLEs were dissolved in hexane:IPA (99:1) and passed through a 0.45 µm PTFE filter by a syringe with a bayonette adaptor.

2.3. Biomarker analysis

Apolar and aromatic biomarker distributions were characterized using a Thermo Scientific™ ISQ Series Single Quadruple GC-MS system. Separation of compounds was carried out on a Zebron non-polar column (50 m x 0.32 mm, 0.10 µm film thickness), with He a carrier gas and an injection volume of 1 µl. The GC programme was: injection at 70 °C (1 min hold), heating to 130 °C at a rate of 20 °C/min, then to 300 °C at 4 °C/min, followed by a 24 min hold. The mass spectrometer continuously scanned between *m/z* 50 and 650, and identification of biomarkers was carried out based on published retention times and spectra.

The distribution of GDGTs in the polar fraction was determined using a High Pressure Liquid Chromatography-atmospheric pressure chemical ionisation-Mass Spectrometry (HPLC-APCI-MS) with a ThermoFisher Scientific Accela Quantum Access triple quadrupole MS in selected ion monitoring mode. Normal phase separation achieved with two HPLC BEH HILIC columns (2.1 mm x 150 mm, 1.7 µm i.d) at a flow rate of 0.2 ml/min. The initial solvent hexane:iso-propanol (IPA) (98.2:1.8) eluted isocratically for 25 min, followed by an increase in solvent polarity to 3.5% IPA in 25 min, and then by a sharp increase to 10% IPA in 30 min (Hopmans et al., 2016). Analysis of isoprenoid and branched GDGTs, was performed using Selection Ion Monitoring (SIM) at *m/z*: 1302, 1300, 1298, 1296, 1294, 1292, 1050, 1048, 1046, 1036, 1034, 1032, 1022, 1020, 1018, 744, 653 to increase the sensitivity and reproducibility.

To reconstruct SSTs we used TEX_{86} (Schouten et al., 2002), (Fig. 5). TEX_{86} is based on the concentrations of GDGT-1, GDGT-2, GDGT-3 (numbers refer to the number of cyclopentane moieities) and the crenarchaeol isomer (Cren′), as defined below:

$$TEX_{86} = \frac{(GDGT-2)+(GDGT-3)+(Cren.\prime)}{(GDGT-1)+(GDGT-2)+(GDGT-3)+(Cren.\prime)}$$

TEX_{86}-based SSTs (Schouten et al., 2002) were determined using both the Deeptime version of the Bayesian Spatially varying Regression (BAYSPAR) with a prior of 30 ± 20 °C and search tolerance of 3 standard deviations (Tierney and Tingley, 2014), as well as the linear calibration of O'Brien et al. (2017). Branched to Isoprenoidal Tetraether (BIT) indices were below 0.05 and frequently 0, indicating the near absence of branched GDGTs.

Compound specific $\delta^{13}C$ values of pristane and phytane (apolar fraction) were determined using an Agilent Industries 7890A gas chromatograph coupled to an IsoPrime 100 GC-combustion-isotope ration MS (GC-C-IRMS) system. Samples were injected onto a capillary column (50 m x 0.32 m, 0.17 µm film thickness) using He for carrier gas. The GC oven temperature programme was the same as for GC-MS analyses. Samples were measured in duplicate and the presented value reflects the mean of duplicates. $\delta^{13}C$ values were converted to Vienna Peedee Belemnite (VPDB) by bracketing with an in-house gas (CO_2) of known $\delta^{13}C$ value. Instrument stability was monitored by regular analysis of an in-house fatty acid methyl ester standard mixture; long-term precision is ± 0.3‰.

2.4. $\delta^{15}N$ analysis

Bulk $\delta^{15}N$ determinations were performed on a Thermo Scientific Flash IRMS Elemental Analyzer, coupled to a Delta V Advantage IRMS through a Conflo IV universal interface. $\delta^{15}N$ values were calculated using the authentic standards USGS40 and USGS41a (both are glutamic acid, purchased from USGS), along with several in-house laboratory standards (glutamic acid and tyrosine). These analyses were performed in Laboratory for Molecular Biogeochemistry and Organic Geochemistry at Harvard University, USA.

2.5. cGENIE model setup

We re-estimated the global extent of deoxygenation during the PETM using the model-data comparison approach developed by Remmelzwaal et al. (2019), supplemented with our new and compiled evidence for photic-zone euxinia. The model employed is the Earth system model of intermediate complexity cGENIE, which couples a 3D ocean biogeochemical model to a 2D atmospheric model (Ridgwell et al., 2007) and which was previously applied to OAE 2 (Monteiro et al., 2012; Naafs et al., 2019) and the PETM (Remmelzwaal et al., 2019). As in Remmelzwaal et al. (2019), we configured cGENIE for the Eocene using bathymetry and continental configuration derived from the higher resolution model FOAM simulations.

We note that the late Palaeocene location of three marine sections (Kheu River, Dzhengutay and Harrell Core) fall into a land grid point of our model. Given the uncertainty of the surrounding paleogeography reconstruction for the Eocene and the large grid cell size of the model, we moved the location of these sites to the nearest marine grid cell. The marginal Peri-Tethyan basins in which the Kheu River, Dzhengtuay and Guru Fatima sediments were deposited are not resolved by cGENIE, nor is the Danish Basin where isorenieratene

derivatives have also been found; as such our data-model comparison can only be indicative, and it is likely that the basins are more sensitive to deoxygenation than simulated. The Arctic Ocean is not resolved in cGENIE and the location of the Arctic IODP Site M0004A was too far away from any ocean grid cells to be adjusted for data-model comparison; however, its response to PETM climate change is essential to understanding biogeochemical feedbacks and is included in the discussion below.

The annual average wind field transformed to the cGENIE grid came from the Eocene FOAM experiment run with 4xCO_2 (relative to the preindustrial atmospheric value). The cGENIE model biogeochemistry accounted for carbon, phosphorus, nitrogen, oxygen and sulphur cycling as described by Monteiro et al. (2012), including equations and parameter values for ocean productivity and ocean productivity temperature control. We ran the model under different environmental forcings, varying ocean phosphate inventory and atmospheric CO_2 to find the best model conditions to reconstruct proxy observations of the ocean redox state.

3. Results and Discussion

3.1. Organic Matter Sources and Thermal Maturity

As previously reported (Dickson et al., 2014b), the apolar fraction of Kheu River sediments contains abundant *n*-alkanes (C_{17}-–C_{35}), isoprenoids (pristane, phytane, lycopane), hopanes (C_{27}-C_{31}, ββ, αβ and βα isomers), and steranes (C_{27}–C_{29}), and subordinate abundances of sterenes. The ratio of the short to long chain *n*-alkanes [C_{17}/(C_{17}+C_{31})] could not be determined in most pre- and post-PETM sediments, but during the PETM it was highly variable with values ranging from 0 to 0.6. The odd-over-even carbon preference index (CPI) of the high-molecular-weight (HMW) *n*-alkanes is low (0.5 to 1) in pre-PETM sediments but higher and variable (1 to 2.5) in the organic-rich PETM interval. This suggests that the organic-rich interval is characterised by relatively fresher organic matter than underlying and overlying layers, with varying contributions from aquatic vs terrestrial sources. The average C_{31} hopane maturity index – 17β,21β(H)/(17β,21β(H) + 17β,21α(H) + 17α,21β(H)) (Mackenzie et al., 1980) – is 0.7, and the degree of C-22 hopane isomerisation, the 22S/(22S+SSR) ratio (Mackenzie et al., 1980), is very low (~0.03). Together, these indicate relatively low thermal maturity. Like CPIs, hopane distributions indicate lower ‘thermal maturity’ in PETM sediments than preceding and overlying sediments; this contrasts with previous studies which showed an influx of petrogenic, thermally mature organic matter during the PETM in Tanzania (Handley et al., 2012; Carmichael et al., 2017) and the US

Mid-Atlantic Coast (Lyons et al., 2018) and appears to instead document dramatically enhanced burial of fresh organic matter during the PETM at this site.

The aliphatic fractions from the Guru-Fatima section contain *n*-alkanes (C_{16}–C_{35}), isoprenoids (pristane, phytane and lycopane), steranes (5α,14α,17α isomers of C_{27}–C_{29} as well as some methyl steranes), and hopanes (C_{27}–$C_{32,}$ dominated by 17α,21β(H) isomers). The short to long chain *n*-alkane ratio [C_{17}/(C_{17}+C_{31})] is ~0.8, and it does not vary significantly between organic-rich and organic-lean horizons. The CPIs of the long chain (C_{25}–C_{37}) *n*-alkanes during the PETM are ~1 and slightly lower than pre- (~1.4) and post PETM (~2) sediments. Overall, this suggests that organic matter is thermally mature and of mixed origin. The C_{31} hopane maturity index is 0 as ββ isomers were not detected in any sample, and the 22S/(22S+SSR) ratio is ~0.4, indicating much higher thermal maturity than Kheu River sediments.

The aliphatic hydrocarbon fractions from Dzhengutay contain *n*-alkanes (C_{16}–C_{35}), isoprenoids (pristane, phytane and lycopane), steranes (5α,14α,17α isomers of C_{27}–C_{29} as well as some methylsteranes), and hopanes (C_{27}–$C_{32,}$ dominated by 17α,21β(H) isomers). The ratio of the short to long chain *n*-alkanes [C_{17}/(C_{17}+C_{31})] could not be determined prior to- and after the PETM, due to low abundances of HMW components; the ratio was relatively variable around 0.8 in the black shale horizon. In the organic-rich PETM intervals, HMW *n*-alkanes have a slight odd-over-even carbon number predominance (CPI~1.4). Similar to Guru Fatima, the C_{31} hopane maturity index was 0 as ββ isomers were not detected, and the 22S/(22S+SSR) ratio is ~0.4, again indicating much higher thermal maturity than Kheu River sediments.

The sediments from Zumaia are the least mature amongst the studied sections here, evidenced by the near absence of steroids and hopanoids in their apolar forms and abundant functionalised compounds. They are organic-lean and dominated by aliphatic components. The *n*-alkanes are characterised by a homologous series of *n*-alkanes, ranging from C_{17} to C_{33}, with most samples being dominated by the HMW components and the C_{17}/(C_{17}+C_{31}) ratios typically being lower than 0.3. However, values are highly variable and higher ratios occur at the base of the CIE in the Siliciclastic Unit. This is consistent with a marginal marine setting strongly influenced by episodic terrigenous organic matter inputs (Dunkley-Jones et al., 2018).

3.1.1. Pristane and Phytane $\delta^{13}C$ Values Confirm High *p*CO2 during the PETM

Pristane (Pr) and phytane (Ph) $\delta^{13}C$ values were measured for Guru-Fatima and Dzhengutay sediments (their abundance was too low in the thermally immature Kheu

sediments and the terrestrially-dominated Zumaia sediments). These isoprenoidal hydrocarbons derive from the phytyl side-chain of chlorophyll and, therefore, are considered to be of algal origin in marine sediments (Volkman and Maxwell, 1986; Li et al., 1995). Although we have limited data (Table 1), the $\delta^{13}C_{Pr}$ and $\delta^{13}C_{Ph}$ values in Guru-Fatima are lowest during the PETM, as expected given the global CIE. Across our two sites $\delta^{13}C_{Pr}$ values exhibit a -4.6 ‰ excursion (from -29.8 to -34.4 ‰), whereas $\delta^{13}C_{Ph}$ values exhibit a smaller –2.9 ‰ excursion (from -30 to -32.9 ‰). At Dzhengutay, pristane and phytane $\delta^{13}C$ values could not be determined in pre- and post-PETM sediments due to their low abundances; however, in the organic-rich PETM horizon, $\delta^{13}C_{Pr}$ and $\delta^{13}C_{Ph}$ values are relatively low, about -35 and -34 ‰, respectively.

Table 1: Carbon isotopic compositions of pristane and phytane in Peri-Tethyan sediments

	Depth[1] (PETM in italics)	**Pristane $\delta^{13}C$ (‰)**	**Phytane $\delta^{13}C$ (‰)**
Guru-Fatima	5.30	-31.7	-30.5
	1.00	*-34.4*	*-33.0*
	0.60	*-34.3*	*-32.8*
	0.30	*-33.9*	*-32.2*
	-1.70	-29.8	-30.1
	-2.70	-31.6	-32.0
Dzhengutay	*0.85*	*-35.4*	*-34.7*
	0.70	*-35.3*	*-34.2*
	0.35	*-34.8*	*-33.5*

[1]Depth is in meters up-section relative to the base of the PETM as inferred from bulk OM $\delta^{13}C$ values

The phytane $\delta^{13}C$ values determined for PETM sediments at both sites are among the lowest observed across the entire Phanerozoic (Witkowski et al., 2018). Pristane $\delta^{13}C$ values are even more negative. Although diagenesis can alter the stable carbon isotopic composition of bulk organic matter by up to 3 ‰ (Hayes et al., 1990), the $\delta^{13}C$ values of individual compounds are expected to be robust (Hayes, 1993). Instead, the difference between these compounds of inferred similar origin could be due to biological factors, deriving from different photoautotroph assemblages with different isotope signatures or an additional (archaeal?) source for phytane that would have dampened the magnitude of its expressed excursion. The recorded CIEs ($\delta^{13}C_{Pr}$ and $\delta^{13}C$) in Guru Fatima are similar to other aquatic or algal-specific records from the PETM. For example, PETM phytane $\delta^{13}C$ values from the Gulf Coastal Plain, Mississippi USA (Sluijs et al., 2014), range from –32 to –34 ‰, although pre-PETM values could not be determined. In the Arctic Ocean, *n*-C_{17} records a –

3.6 ‰ CIE (Pagani et al., 2006). In the North Sea and Arctic, glycerol dipiphytanyl glycerol tetraether lipids (GDGTs) record a –3.6 ‰ CIE (Schoon et al., 2013). Elling et al. (2019) extended this work, showing a consistent –3 to –4 ‰ excursions in the GDGT crenarchaeol from the New Jersey Shelf, Tasman Sea and Arctic Ocean. Carbon isotopic analysis of single-species dinoflagellate cysts record a CIE between –2 and –4 ‰ (Sluijs et al., 2018). The modest sample numbers in our study and the lack of a corresponding inorganic carbon isotope record causes us to stop short of calculating carbon isotope fractionation, and therefore, pCO_2 (e.g. Witkowski et al., 2018). However, the very low values we find in our sections are consistent with high pCO_2 estimates from previous investigations (Anagnostou et al., 2020).

3.2 Reconstruction of Sea Surface Temperature

We use the Tetraether Index of 86 carbon atoms (TEX_{86}), based on the distribution of isoprenoid glycerol dibiphytanyl glycerol tetraethers (isoGDGTs), to reconstruct SSTs during the PETM. Isoprenoidal GDGTs are widespread in marine environments but mainly biosynthesised by the dominant group of marine planktonic Thaumarchaeota now Nitrososphaerota (See review Schouten et al., 2013). TEX_{86} is widely used to reconstruct SST, including at the PETM (Sluijs et al., 2006, 2011, 2014; Frieling et al., 2014, 2019). However, it has yet to be applied to Peri-Tethyan settings, and in fact there are few SST reconstructions from this region using any proxy (Frieling et al., 2014).

GDGTs were only detected in Kheu River samples, and only in the PETM and post-PETM sediments. GDGT distributions are sensitive to thermal maturation, becoming skewed when hopane $\beta\beta/(\beta\beta+\alpha\beta+\beta\alpha)$ ratios decline below 0.5, and they are degraded at higher thermal maturity (Schouten et al., 2004). Therefore, the absence of GDGTs in Guru-Fatima and Dzhengutay is likely caused by the high thermal maturity of these sediments. However, Kheu River sediments are less mature, with hopane $\beta\beta(/\beta\beta+\alpha\beta+\beta\alpha)$ ratios >0.5 (~0.6 and ~0.8 in post-PETM and PETM sediments, respectively), and TEX_{86} is expected to be robust. Other factors that impact TEX_{86} validity are high inputs of terrestrial GDGTs (Weijers et al., 2006) and contributions from benthic Archaea, including methanogens and anaerobic methanotrophs (Pancost et al., 2001). These factors are precluded by low Branched to Isoprenoid Tetraether (BIT) and Methane Indices (MI) (ca. 0 and <0.15, respectively).

The balance between deep and shallow Thaumarchaeota contributions to sediments is recorded by isoGDGT-2 to isoGDGT-3 ratios (Taylor et al., 2013). A shallow signal is documented by 2/3 ratios < 4 (Rattanasriampaipong et al., 2022), which we observe for all of

our PETM sediments from Kheu River. However, the post-PETM sediments have higher 2/3 ratios (4.1, 4.5 and 12, respectively), similar to those found in most open marine sections today and suggesting contributions from deeper-dwelling Thaumarchaeota. This change is probably not due to a rapid deepening of the basin given the timescales involved, and instead appears to reflect changes in export dynamics. Intriguingly, previous work (Rattanasriampaipong et al., 2022) also documents low 2/3 ratios during times of organic-rich sediment accumulation and inferred water column anoxia. However, we note that interpretation of these changes must be done cautiously at high TEX_{86} values where the %GDGT-1 is low, such that the TEX_{86} response to temperature must become increasingly dependent on decreasing %GDGT-2.

TEX_{86} values at Kheu River are very high, often exceeding 0.95, in PETM sediments and somewhat lower (about 0.8) post-PETM. The organic lean nature of the pre PETM sediments precluded TEX_{86} determination. Multiple calibrations have been developed for the SST- TEX_{86} relationship, and here we use a linear calibratioin and the DeepTime BAYSPAR calibration. Because both assume linear relationships, both yield very high PETM temperatures often in excess of 40 °C; these should be viewed with caution as such temperatures are outside the range of the training data. These are among the highest TEX_{86} values and inferred SSTs yet documented for the PETM, being slightly higher than even those from the New Jersey Shelf PETM (0.92 to 0.95; Elling et al., 2019). Lower temperatures of 33 to 37°C are calculated for the three post-PETM sediments.

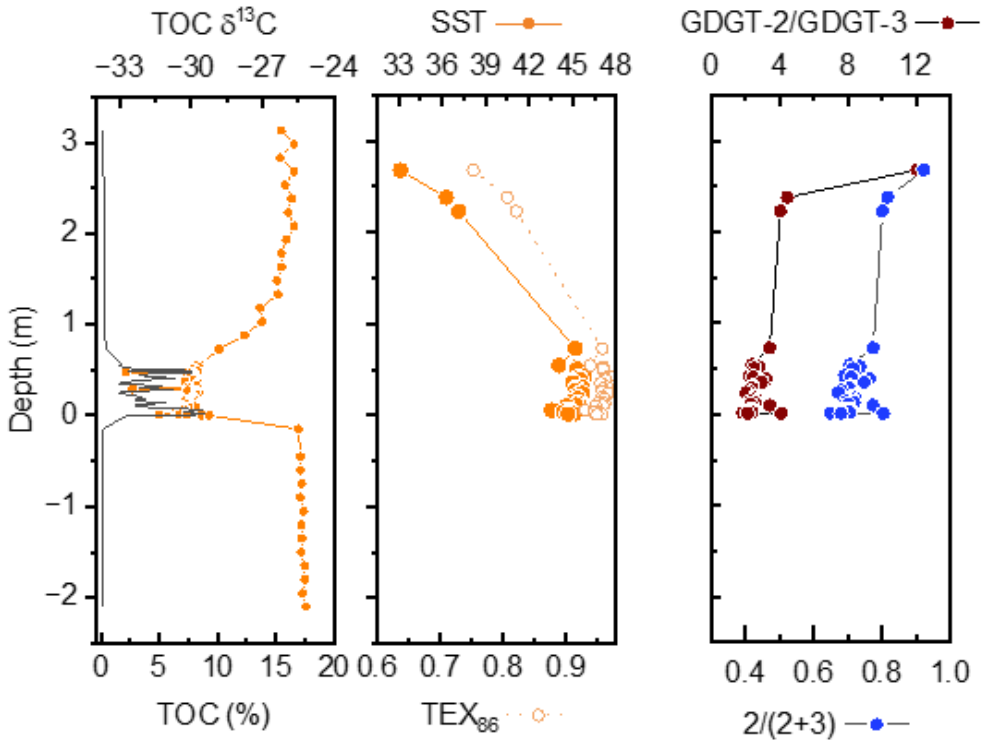

***Figure 2**. TOC contents and $\delta^{13}C$ values and GDGT ratios from the Kheu River Section. TEX_{86} values are shown with the associated SSTs derived from the linear calibration of O'Brien et al (2017); BAYSPAR- and TEX_{86}^{H}-derived SSTs are included in the SI. Also shown are GDGT-2/GDGT-3 ratios expressed in both the originally proposed 2/3 form and the linear 2/(2+3) form.*

Our PETM SST record is novel in the Tethyan mid-latitude (Kheu River paleolatitude ~ 40°N) and Peri-Tethys region. It documents a substantial SST cooling after the PETM, as has been inferred before in other PETM sections based on both TEX_{86} and other proxies (e.g. Zachos et al., 2006; Sluijs et al., 2006, 2014; Frieling et al., 2014). The estimated cooling of ~8-10 °C is dramatic but similar to TEX_{86} PETM records from the mid-latitude Atlantic. For example, an increase in TEX_{86} from 0.75 to 0.95 at the New Jersey Shelf (Ancora Core, Elling et al., 2019) represents a >10°C warming. The Mississippi Harrell Core, Gulf Coastal Plain ~32°N (Sluijs et al., 2014), records a 7 °C warming, but that study applied the less sensitive sigmoidal TEX_{86}^{H} calibration. We note, however, that the apparent cooling at Kheu River could have been enhanced by changes in the thermocline or export dynamics as suggested by the change in isoGDGT 2/3 ratios.

3.3 Biomarker evidence for water column anoxia and photic zone euxinia

The Peri-Tethyan sites contain a variety of biomarkers indicative of water column anoxia or euxinia, including lycopane and isorenieratane (Fig. 3). The source of lycopane remains unclear, but it is strongly associated with dysoxia in the modern ocean (Sinninghe Damsté et al., 2003). At Kheu River (Fig. 4), as previously reported (Dickson et al., 2014b), lycopane ratios are variable but high in PETM organic-rich sediments (up to a value of 2), whereas ratios are low in pre- and post-PETM horizons (< 0.5). At Guru Fatima, lycopane ratios are as high as 0.8 during the PETM (Fig. 4) but markedly lower (< 0.3) in the pre- and post-PETM sediments. In the Dzhengutay section the ratio is ~0.5 during the PETM and lycopane is absent (ratio = 0) in pre- and post PETM samples. The sediments from Zumaia contain no lycopane (ratio = 0) prior to or during the PETM.

The two to fourfold increase in lycopane ratios during the PETM across the three NE Peri-Tethys marginal sections indicates increased water column deoxygenation. Moreover, the ratios during the PETM at all three NE Peri-Tethys sites (values between 0.5–2) are much higher than those observed in modern oxygenated settings and similar to those at locations with strong and persistent OMZs, e.g. the Arabian Sea (ratio ~0.8) (Schulte et al., 1999; Sinninghe Damsté et al., 2003) and Peruvian Shelf (ratio ~2.5) (Farrington et al., 1988; Sinninghe Damsté et al., 2003). They also are similar to those observed in late Cretaceous OAE3 black shales (Wagner et al., 2004). The higher values at Kheu River suggest that this site might have experienced the most pronounced water column anoxia, although this could also be a consequence of its lower thermal maturity as isoprenoidal hydrocarbons will crack more readily than straight-chain components (Summons et al., 1988).

In addition to high lycopane ratios, sediments from the three NE Peri-Tethys marginal sections all contain isorenieratane, plus isorenieratene derivatives bearing additional aromatic rings and lower-carbon-number pseudo-homologues that arise from aromatic ring expulsion (Koopmans et al., 1996) (Fig. 3). This suite of biomarkers only occurs in the PETM intervals, being absent or below detection in all pre- and post-CIE (PETM) sediments (Fig. 4). Isorenieratane concentrations in the NE Peri-Tethys marginal settings vary between sites. Concentrations are highest at Guru Fatima (Figure 4), varying between 50 to 200 µg g^{-1} sediment, but we note that exceptionally high metal concentrations at Guru Fatima could be evidence for sedimentary condensation. Lower concentrations occur at Dzhengutay (~0.01 µg g^{-1} sediments). Concentrations at Kheu River are intermediate (~0.5 µg g^{-1} sediments) but display stratigraphic structure with the highest concentration of isorenieratane occurring in the basal PETM sediments before decreasing to concentrations similar to those at Dzhengutay. Given the much higher resolution of our data from the

former, we cannot preclude similar patterns at the other sites. The Kheu River observation also aligns with high-resolution analyses indicating that highest organic matter burial was associated with a basal saproletic bed that coincides with the onset and peak of the CIE but not its recovery (Shcherbinina et al., 2016). We also caution that these concentrations do not include the S-bound component of isorenieratene derivatives, which can be significant especially in organic-rich, low thermal maturity sections; indeed, Schoon et al. (2015) found significant S-bound concentrations of isorenieratene in shallow marine PETM sections from Denmark.

Regardless of the between-site differences, our new biomarker data provide clear evidence that water column anoxia occurred throughout the NE Peri-Tethys marginal settings during the PETM, and it provides the first comprehensive evidence that this was accompanied by intense and regionally extensive PZE. The highest concentrations at Guru Fatima are comparable to those observed in the Atlantic during Mesozoic OAEs (Kuypers et al., 2002; Pancost et al., 2004). Given the neritic setting, it is possible that the PZE has occurred in the lower part of shallow (100-200 m) water columns, although the high GDGT-2/GDGT-3 ratios in some samples appear to preclude that (Taylor et al., 2013). These observations are consistent with and expand on multiple lines of evidence that indicate a decrease in water column oxygenation during the PETM in the northern margins of Peri-Tethys, as well as evidence that the intensity of anoxia was strongest further to the east. These include elevated TOC contents, including some of the highest observed for the PETM (Dickson et al., 2014b; Gavrilov et al., 2003); high and dynamic abundances of redox sensitive elements, such as molybdenum (Mo), rhenium (Re), and highly reactive Fe; and remobilisation of reactive phosphorus (Dickson et al., 2014b). In contrast to the NE Tethys sites, open-margin Zumaia sediments do not contain lycopene or isorenieratene derivatives, even during the PETM, indicating that this region did not experience water column anoxia nor PZE – although planktic foraminiferal faunal turnover has been invoked as evidence for development of suboxic conditions in an oxygen minimum zone (Canudo et al., 1995; Molina et al., 1999).

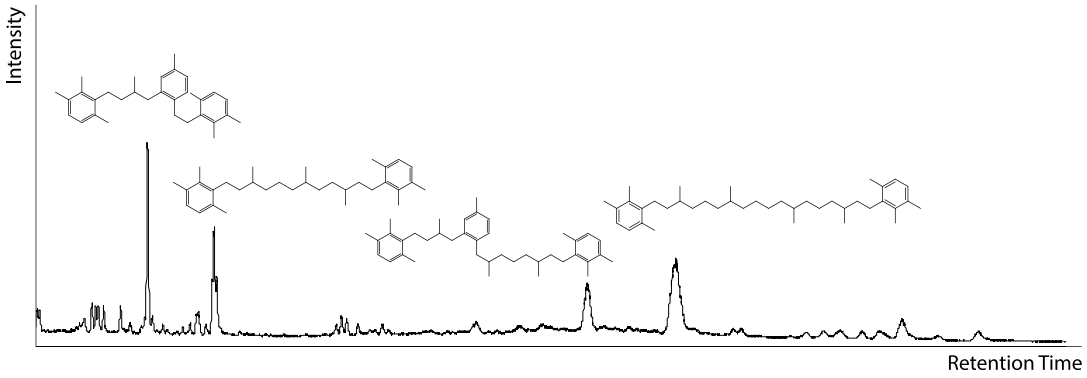

524

525 ***Figure 3*** *Partial m/z 133 + 134 chromatogram obtained from GC-MS. Isorenieratane and*
526 *other diagenetic products of isorenieratene are highlighted in an example of aromatic*
527 *fraction from Guru-Fatima PETM sediments.*

528

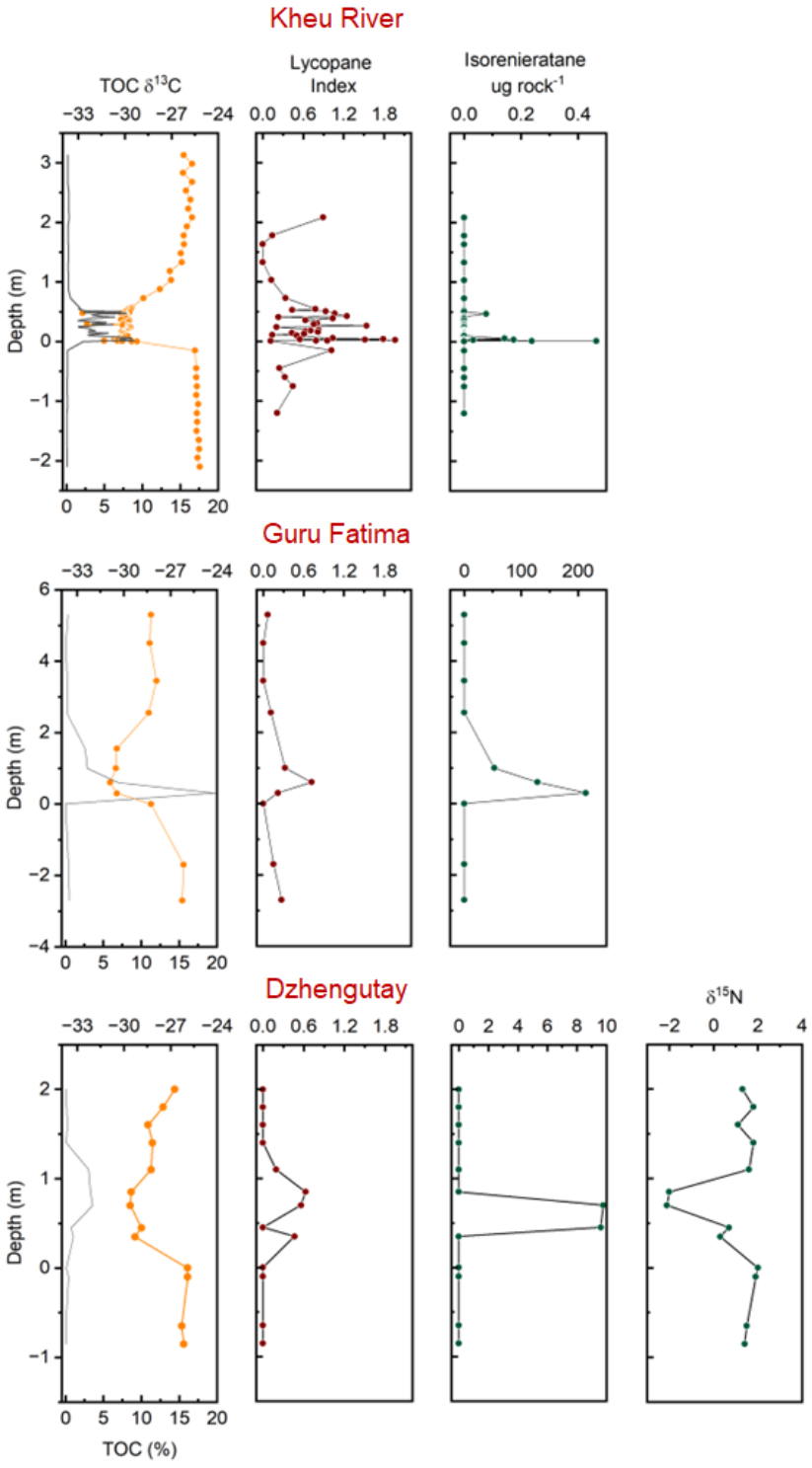

529

530 ***Figure 4.*** *Organic geochemical data from Peri-Tethyan sites: bulk organic carbon* $\delta^{13}C$
531 *values and TOC contents, lycopane indices, and isorenieratane concentrations in the Kheu*
532 *River, Guru-Fatima, and Dzhengutay Sections. Also shown are bulk organic matter* $\delta^{15}N$
533 *values from Dzhengutay.* $\delta^{13}C$ *data are taken from Dickson et al (2014b) and relative depths*
534 *in Kheu River, Dzhengutay and Guru-Fatima are based on the onset of the PETM CIE. Note*

that all geochemical indices are plotted on the same scale across the three sites, except for isorenieratane concentrations.

3.3.1. Organic matter $\delta^{15}N$ values

Additional evidence for changes in water column redox conditions that impacted biogeochemical cycles comes from bulk $\delta^{15}N$ analyses. A common feature of OAE 2 sediments are low organic $\delta^{15}N$ values (< 2‰) that decrease across the OAE (Junium and Arthur, 2007). The causes for this are contested, with early work proposing that it reflects increased N_2 fixation (Junium and Arthur, 2007), but more recent papers arguing that it reflects a combination of N_2 fixation and increased ammonia utilisation (Higgins et al., 2012; Junium et al.,, 2018; Naafs et al., 2019). Similar $\delta^{15}N$ shifts have been reported for the PETM from the Arctic Ocean (from 3 to 1‰; Knies et al., 2008) and Kheu River (from 4 to -2‰; Junium et al., 2018). We see a similar shift from 2 to -2‰ at Dzhengutay. We could not determine pre-PETM $\delta^{15}N$ values at Guru Fatima, but PETM values are ~0 ‰ and post-PETM values are ~1 ‰.

3.4. Model-data comparison to explore driving mechanisms for anoxia

We test the effect of pCO_2 (via its impact on temperature) and ocean nutrient (phosphate) inventory on ocean redox in the cGENIE model of Remmelzwaal et al. (2019). We do not replicate the comprehensive data-model comparison of Remmelzwaal et al. (2019). Instead, we further assess the patterns and drivers of marine deoxygenation across the PETM that are consistent with Peri-Tethyan PZE and water column anoxia (Fig. 5).

PETM simulations with elevated ocean phosphate generate PZE in a wide range of locations with the eastern Peri-Tethys being particularly sensitive (Fig. 5). Simulations with 1 x PO_4 (or more) generate PZE in the Peri-Tethys, consistent with the observed presence of isorenieratane at all three sites during the PETM (as well as Kurpai, Gavrilov et al., 2003). The 1xPO_4 simulation also generates PZE in the Dahmay Basin (Frieling et al., 2017), showing the sensitivity towards deoxygenation of NE Peri-Tethys marginal settings and the equatorial South-East Atlantic to nutrient changes. However, the cGENIE model fails to show the development of PZE in the Western North Atlantic as expressed in the PETM sediments of the Gulf Coastal Plain (Harrell Core) (Sluijs et al., 2014). This discrepancy could arise if PZE was only intermittent, as suggested by the same authors based on the presence of glauconite and organic linings of benthic foraminifera. Alternatively, cGENIE

predicts low H_2S concentrations for adjacent grid cells at high $2xPO_4$ loading, suggesting that this area is sensitive to deoxygenation but not to the same degree as the Peri-Tethyan areas. The relatively coarse spatial resolution of cGENIE, therefore, could be affecting the results. Nor does cGENIE generate PZE in the NE Atlantic, the nearest marine grid cell to the Danish Basin (Schoon et al., 2015). This likely reflects the restricted nature of the actual basin that allowed a more pronounced deoxygenation than the cGENIE simulated open ocean. Therefore, most but not all PETM indicators of photic zone euxinia can be simulated by modest increases in the global ocean phosphate inventory from 0.5x to 1x the modern inventory. Higher phosphate inventories ($2 \times PO_4$), analogous to the increases required to simulate aspects of OAE2 deep ocean anoxia (Monteiro et al., 2012), result in widespread PZE that is inconsistent with observations.

The increase in PO_4 required to generate PZE in the Peri-Tethys (from 0.5x to 1x current concentrations) differs slightly from the findings of Remmelzwaal et al. (2019), in which i) $1xPO_4$ was consistent with both pre-PETM and PETM bottom water oxygen and ii) an increase in temperature driven by an increase from $2xCO_2$ to $6xCO_2$ was sufficient to explain the modest bottom water deoxygenation. However, the expansion of PZE documented by our new data can only be simulated by an increase in nutrients. An increase from 0.5x to 1x current concentrations also yields a larger simulated increase in bottom water deoxygenation during the PETM (data not shown), but that remains consistent with the proxy data. Although not the primary driver (Fig. 5), the high SSTs during the PETM and especially in the Peri-Tethys likely contributed to deoxygenation of the surface oceans via lower oxygen solubility and increased rates of organic matter remineralisation, consistent with our previous simulations for OAE 2 (Monteiro et al., 2012). However, elevated SST is neither necessary to explain our observations nor is it sufficient to explain them in the absence of elevated nutrient inventories.

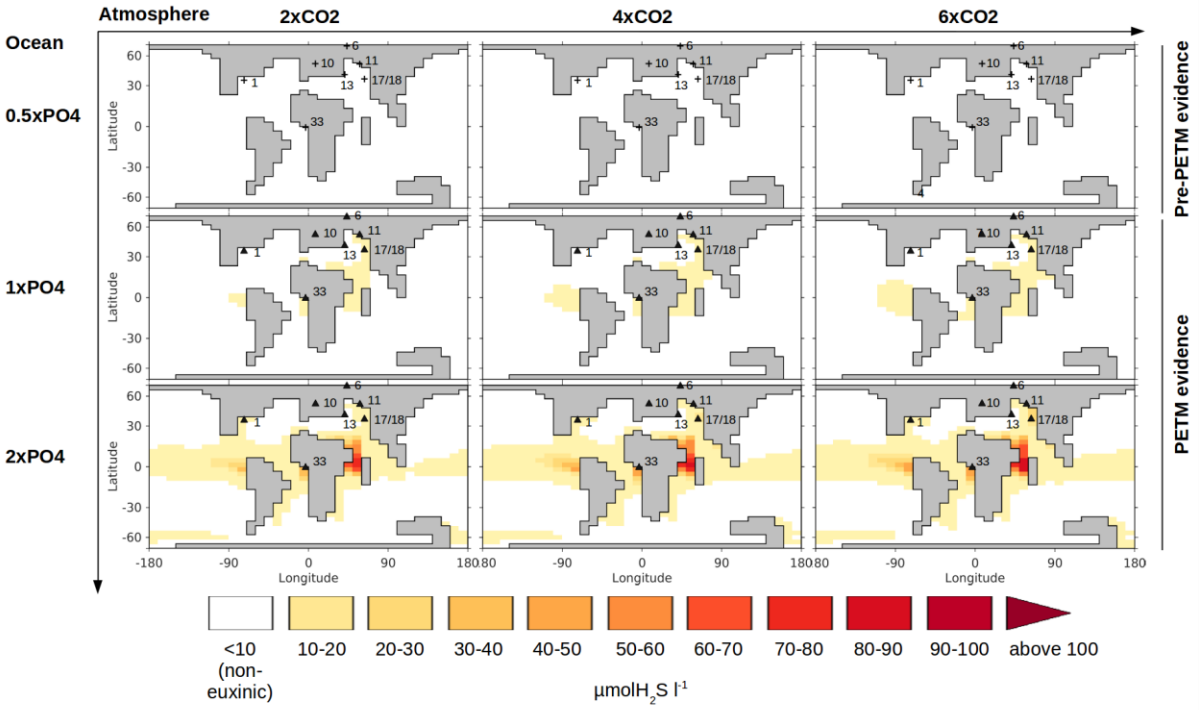

Figure 5. *cGENIE model-data photic zone (80-200 m) hydrogen sulfide reconstruction for inferred pre-PETM (0.5x modern PO_4 inventory) and during PETM (1 and 2x modern PO_4 inventory) periods. This reconstruction is based on that of Remmelzwaal et al. (2019) completed with the photic zone euxinia data points from this study. Isorenieratane evidence for photic zone euxinia is shown by filled triangles and its absence at the same sites prior to the PETM depicted with a (+); note however, that isorenieratane concentrations vary dramatically between sites, and sites that fall into the land mask of the model due to its low resolution are included for indicative purposes. Site numbers are the same as in Figure 1: 1) Gulf Coastal Plain (Harrell Core; Sluijs et al., 2014); 6) Arctic Ocean (IODP Site M0004; Sluijs et al., 2006); 10) North Sea (Store Baelt; Schoon et al., 2015); 11) West Siberian Sea (Well 10; Frieling et al., 2014); 13) North Central Peri-Tethys (Kurpai and Guru Fatima; Gavrilov et al., 2003 and this paper); 17/18) North East Per-Tethys (Kheu River and Dzhengutay; this paper); 33) Eastern Shelf of the South Atlantic (Dahomey Basin, Frieling et al., 2017).*

3.4.1. Why was water column anoxia and euxinia pronounced in the Peri-Tethys?

The presence and in some cases high concentrations of isorenieratane in the northern Peri-Tethys together with high lycopane ratios indicate the establishment of persistent water column anoxia and PZE during the PETM in this region. Interestingly, the highest concentrations of isorenieratane appear to occur in the lowermost part of the PETM CIE,

615 consistent with PZE being a direct response to climate and biogeochemical change initiated
616 by the rapid onset of warming. The episodic nature of anoxic conditions in the PETM Para-
617 Tethys has been attributed to variable water column ventilation (Dickson et al., 2014b, 2012;
618 Friedrich, 2010; Sluijs et al., 2014), but the cyclic nature of anoxia in the western part of the
619 basin could also result from astronomically controlled variations in the climate system, for
620 example modulation of terrestrial nutrient inputs by the hydrological cycle (Carmichael et al.,
621 2017; Gavrilov et al., 2009).

622 Our model simulations allow us to explore why the particular geographical restriction
623 of the Peri-Tethys was more sensitive to nutrient inputs and developed intense PZE relative
624 to other PETM ocean basins. Such mechanisms must account for: (a) the widespread
625 deoxygenation of the Peri-Tethys water column; (b) apparently stronger and more persistent
626 anoxic conditions along the eastern and northern margin (Dickson et al., 2014b; Gavrilov et
627 al., 2003; Junium et al., 2018); and (c) a trend towards less persistent and apparent episodic
628 (or cyclical) anoxia in the NE Peri-Tethys from East to West. Under elevated nutrient
629 concentrations, PZE is present in the eastern part of the Peri-Tethys Sea (Fig. 5). This
630 corresponds to a region of surface upwelling in the model, which brings H_2S from deeper
631 euxinic oxygen minimum zones (OMZs) to the surface (Fig. 6). These large OMZs around
632 the depth of the thermocline (400–700 m) (Fig. 6b and 6d) are fuelled by intense organic
633 material remineralisation.

634 According to the model, the Peri-Tethys is more prone to euxinia than other regional
635 seas at these depths (Figure 6d), likely due to the slow exchange of waters with the Atlantic
636 and Indian Oceans, which would otherwise provide oxygen to this basin. Sensitivity model
637 experiments show that deepening of the gateway between the Peri-Tethys Sea and the
638 Indian Ocean results in a reduction of Peri-Tethys water column H_2S concentration (Fig. 7);
639 this is not observed when deepening the gateway between the West Peri-Tethys and North
640 Atlantic basin (data not shown). We note that PETM Os(i) ratios in two previously studied
641 Peri-Tethys sites are similar to those of the open ocean, indicating that it was not restricted,
642 at least not to the same degree as the Arctic Ocean, at this time (Dickson et al., 2022). As
643 such, the gateway does not appear to be a driver of deoxygenation but is instead a pre-
644 condition, explaining why PETM organic-rich sediments are abundant in this region and
645 apparently sensitive to climatic variability.

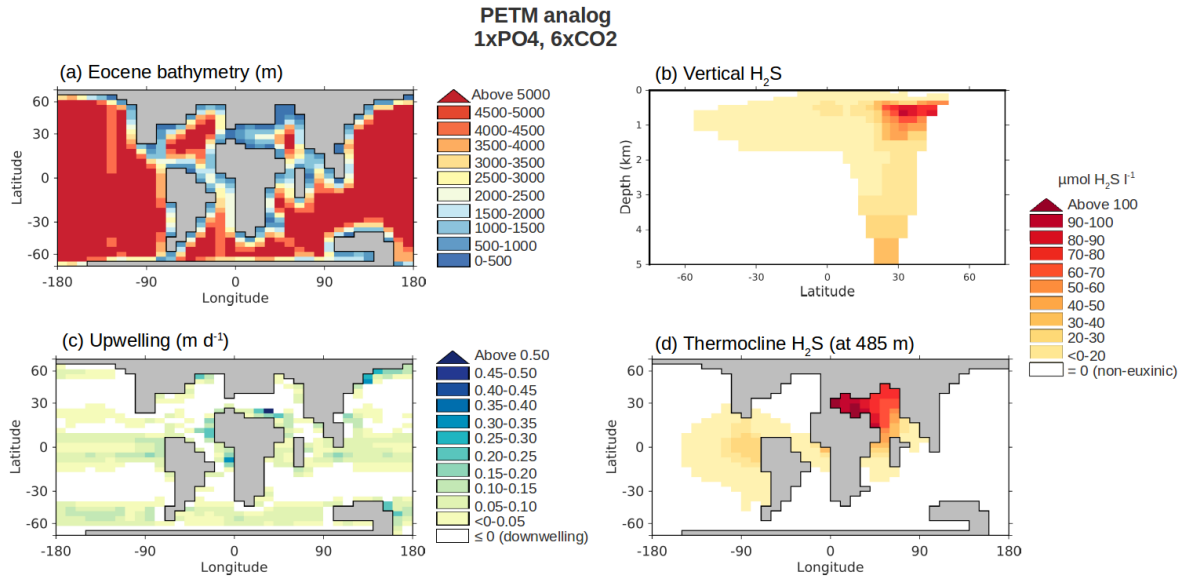

Figure 6. *H_2S distribution during the PETM as a function of paleogeography and upwelling. The presence of PZE often corresponds to the regions of surface upwelling in the model: (a) bathymetry in the PETM model simulation (Eocene; m); (b) zonally averaged vertical H_2S distribution during the PETM (µmol l^{-1}); (c) location and intensity of upwelling during the PETM; and (d) distribution of euxinia at the depth of the thermocline (400-700 m). Note the particularly strong thermocline euxinia simulated for the Tethys Sea.*

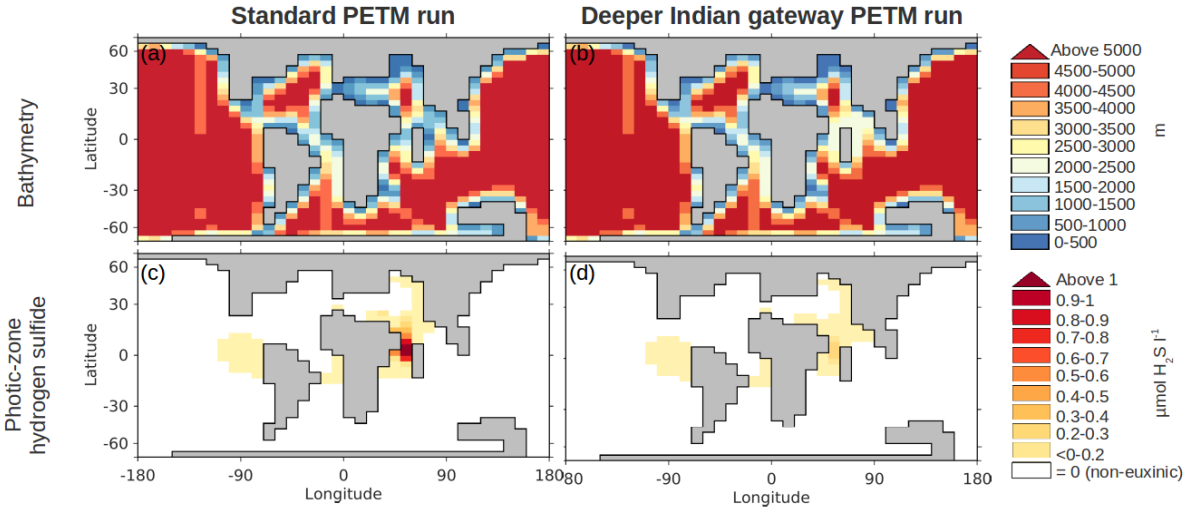

Figure 7. *Sensitivity experiments on PZE in the Tethys Sea due to the deepening of the Indian gateway. (a) and (b) bathymetry for the standard simulation (1 x PO_4 and 6 x CO_2) and with Indian gateway deepened to 1900 m; (c) and (d) photic-zone H_2S concentration for the standard and deeper Indian gateway simulations. Note the change of scale with Figures 5 and 6 to highlight the changes in H_2S during the 2 experiments.*

3.5 Biogeochemical Comparisions between Mesozoic OAEs and the PETM

The ability of cGENIE to reproduce global trends in PETM deoxygenation (Remmelzwaal et al., 2019) as well as regional patterns of PZE (this work) gives confidence in its application to interrogating mechanisms for deoxygenation and drawing comparisons with OAE2 (Monteiro et al., 2012). In order to achieve PZE in the Peri-Tethys, cGENIE requires phosphate loadings that also bring about globally widespread bottom water deoxygenation, albeit little anoxia (Remmelzwaal et al., 2019), indicating a strong coupling between regional and global responses to nutrient forcing even though the magnitude of regional responses are highly variable. This relationship could be exaggerated as cGENIE lacks a sediment module, such that nutrients cannot be permanently sequestered in anoxic basins. Although sedimentary sequestration of phosphate is mitigated by its mobilisation under reducing conditions (van Cappellan and Ingall, 1996), anoxia in the model also will be over-represented by failing to capture how the sequestration of trace metal nutrients impacts primary productivity (Owens et al., 2016; Robinson et al., 2019). Consistent with cGENIE simulations, the global PETM compilation of Papadomanolaki et al. (2022) provides compelling evidence for globally widespread but limited intensity of deoxygenation at the PETM (Fig. 1). Most sites experienced some degree of bottom water deoxygenation, with hypoxic conditions occurring in some open ocean sites and most continental shelf and slope sites. Relatively few sites, however, became anoxic (limited largely to the Peri-Tethys, Arctic Ocean, the North Sea and some sites from the New Jersey and North African shelves). This is also consistent with the lack of an excursion in carbonate-hosted uranium isotopes (Clarkson et al., 2021), which constrains the expansion of seafloor anoxia to <2% of the ocean.

Despite the lack of widespread bottom water anoxia, our simulations do yield widespread euxinia in oxygen minimum zones, especially in restricted, equatorial and upwelling regions (Fig. 7). This supports the findings of Yao et al (2018), who identified a transient 1 ‰ positive excursion in marine sulfate (barite) $\delta^{34}S$ values. The magnitude of the excursion indicates widespread sulfate reduction, whereas the rapid return to pre-PETM values led the authors to conclude that the sulfide must be stored in a reservoir that could be rapidly remobilised. Numerical models suggested that their observations could be explained by a 10-20x increase in the area of oxygen minimum zones (O_2 < 20 mM), consistent with our putative PETM scenario. They are also consistent with molybdenum isotope values that

indicate that the extent of euxinia during the PETM was greater than today but more restricted compared to the Mesozoic OAEs (Dickson., 2017).

Therefore, cGENIE can successfully reproduce geochemical and palaeontological evidence for bottom water deoxygenation and water column sulfate reduction, as well as the geographical distribution of photic zone euxinia and bottom water anoxia. This is achieved by increasing the ocean phosphate inventory, with temperature having only a secondary effect. An increased nutrient inventory at the PETM was likely a feedback response, arising from elevated pCO_2 and temperature and the associated hydrological changes that collectively enhanced erosion and weathering (e.g. Carmichael et al., 2017). These mechanisms are analogous to those proposed for OAE 2 (Jenkyns et al., 2010), supported by recent Li isotope analyses that document comparable OAE 2 and PETM chemical weathering responses (Pogge von Strandmann et al. 2013 and 2021). Alternatively, sea level rise at the PETM (Sluijs et al., 2008) could have remobilised nutrients from the continental shelf.

The PETM has been considered a 'failed' or 'weak' OAE with similar conditions and driving mechanisms as invoked for the Mesozoic OAEs (Jenkyns, 2010; Junium et al., 2018). Although Mesozoic OAEs exhibit a variety of responses, OAE2 was certainly characterised by more extreme water column deoxygenation and more globally widespread seafloor anoxia and PZE compared to the PETM. OAE2 deoxygenation caused increased global organic carbon burial, indicated by the widespread deposition of black shales and the diagnostic positive carbon isotope excursion of the Cenomanian-Turonian Boundary. Consistent with our observations of less severe deoxygenation, the PETM lacks a positive CIE and unambiguous evidence for globally increased OM burial. However, the return to pre-PETM ocean-atmosphere $\delta^{13}C$ values could have been driven by increased OM burial (John et al., 2008; Bowen and Zachos, 2010), especially in restricted basins and on continental margins (Papadomanolaki et al., 2022), i.e. OM burial did increase although not to the same degree as during OAE2, and it contributed to drawing down pCO_2 and a return to pre-CIE conditions. The immature and unaltered character of OM in the Peri-Tethys sites studied here indicates that increased PETM OM burial was due not only to higher sedimentation rates (John et al., 2008) but also enhanced primary productivity and OM preservation under reducing conditions in marginal basins. However, we caution that this enhanced OM burial, at least in the Peri-Tethys, occurred primarily at the onset of the CIE (Shcherbinina et al., 2016) rather than during its recovery and has been linked to regional sea level rise and nutrient mobilisation. Consequently, the interplay of climate change, productivity, anoxia, and carbon cycle dynamics requires further examination.

729 Nonetheless, our model simulations show that the same mechanism – an increase in
730 the oceanic phosphate inventory potentially in response to warming and hydrological
731 change, leading to an increase in weathering and nutrient delivery to the ocean – could have
732 driven water column deoxygenation during the Mesozoic OAEs (at least OAE2) and the
733 PETM. The primary difference in our simulations is that the starting state of the PETM
734 perturbation had a lower ocean phosphate inventory compared to OAE2 and the increase at
735 the PETM was smaller, resulting in less severe deoxygenation. Consequently, only
736 geographically restricted parts of the PETM ocean experienced persistent and strong
737 seafloor anoxia and PZE. These are analogous to lower phosphate loadings in Mesozoic
738 OAE simulations that only generate bottom water anoxia in the North Atlantic (Monteiro et
739 al., 2012).

740 The reason(s) for the inferred difference between OAE2 and PETM nutrient pre-
741 conditions (phosphate inventory) is unclear. Higher Cretaceous PO_4 inventories could reflect
742 higher global weathering rates due to higher Cenomanian temperatures (O'Brien et al.,
743 2017), although this could have been offset by low topographic relief (Goddéris et al., 2014).
744 More speculatively, a higher Cretaceous ocean nutrient inventory could reflect different
745 climate – weathering – marine nutrient relationships arising from global biotic change and
746 significant changes in the terrestrial biosphere during the late Cretaceous (e.g., Taylor et al.,
747 2009).

748 Alternatively, the sensitivity to deoxygenation for a given PO_4 inventory could have
749 differed between the Cretaceous and Palaeogene in ways that are not captured by our
750 cGENIE simulations. In simulations for both time periods, similar PO_4 inventories yield
751 similar global ocean oxygen contents. Thus, geography only dictates the regional distribution
752 of deoxygenation not its global magnitude. Instead, our concluded differences between
753 OAE2 and the PETM arise from the more widespread evidence for bottom water (and in
754 some regions, water column) dysoxia and anoxia during the pre-OAE 2 Mesozoic (Monteiro
755 et al., 2012). These OAE2/PETM differences could potentially reflect more restricted
756 circulation in OAE2 (reducing ocean interior oxygen ventilation), the effects of which are not
757 fully accounted in the low-resolution cGENIE model. Alternatively, the difference could arise
758 from ocean trace metal inventories, as our simulations assume only phosphate and nitrate
759 as biolimiting. Owens et al. (2016) showed dramatic trace metal drawdown during OAE2, but
760 similar evidence for a global drawdown at the PETM is lacking – and perhaps not expected
761 given the lack of global organic matter burial. If background trace metal concentrations were
762 higher during the Cretaceous, they could have sustained a more protracted productivity
763 increase for a given phosphate inventory during OAE2. A third possibility is that the
764 Cretaceous could have had a more sensitive relationship between nutrient inventories,

765 primary productivity and export productivity arising from different planktonic assemblages
766 (e.g. Bown et al., 2005). It is likely that the differences arise from the intersection of these
767 processes, i.e. phosphate mobilisation from sediments or trace metal depletion occurring in
768 geographically restricted basins.

769 Regardless of these mechanisms, the differences between the PETM and OAE2 could
770 reflect a long-term change in the the global biogeochemical response to global warming. In
771 fact, the PETM appears in some respects to be an intermediate scenario between OAE2 and
772 the Middle Miocene, where the classical Monterey Event documents enhanced burial of
773 organic-rich sediments on Pacific Ocean margins (Miller et al., 1991) but the global ocean
774 appears to have become more oxygen-rich (Hess et al., 2023). This has important
775 implications for how inferences from the geological record for biogeochemical responses to
776 climate change should be applied to future warming scenarios. Future work, therefore,
777 should focus on higher resolution simulations to better capture the impact of geography on
778 ocean circulation but also explore how biogeochemical feedbacks evolved over the past 100
779 million years.

780

781 **4. Conclusion**

782 In summary, the marine deoxygenation during the PETM appears to require
783 increased nutrient inputs (doubling phosphate) that stimulated primary productivity and
784 subsequently deoxygenated the water column. CO_2-driven warming likely had an indirect
785 role as the driver of increased nutrient inputs, but its direct impact was minimal; it could have
786 contributed but it is not necessary to explain the observed changes. The pronounced PZE in
787 the Peri-Tethys arose from the interaction of this oxygen depletion with the specific basin
788 geometry, including regional remobilisation of terrestrial nutrients. Temporal variability in
789 isorenieratane and lycopane concentrations across the PETM could be driven by changes in
790 the hydrological forcing of chemical weathering and/or changes in ocean upwelling intensity.
791 The former processes, via a pulse of weathering in response to the PETM initial warming (or
792 sea level rise), could also explain the higher isorenieratane abundances directly after the
793 onset of the negative CIE. This work, by highlighting a common control on Mesozoic OAE
794 and PETM marine anoxia, confirms that warming persistently results in ocean deoxygenation
795 through the indirect mechanism of increased nutrient delivery to the oceans. However, the
796 magnitude and geographical focus and extent of anoxia will depend on a variety of factors
797 including the climatic and biogeochemical processes that mediate the warming – chemical
798 weathering – nutrient flux feedbacks.

Open Research

All geochemical data are provided in the supplementary information that accompanies this manuscript. Upon acceptance, they will also be uploaded to Pangaea. The model code for the version of the GENIE model used in this paper (technically: cGENIE) will be uploadedt to github and include all configuration and boundary condition files needed to carry out the spin-ups, the control experiments, and all parameter variation experiments used in this manuscript. Documentation on running the cGENIE model can be found in the genie-docs directory of the code installation.

Acknowledgment

This research was funded through the advanced ERC grant "The Greenhouse Earth System" (T-GRES, project reference 340923), awarded to RDP. B.D.A.N. acknowledges additional funding through a Royal Society Tata University Research Fellowship. The authors wish to thank NERC for partial funding of the mass spectrometry facilities at Bristol (contract no. R8/H10/63; www.lsmsf.co.uk). F.M.M. acknowledges NERC funding (ANAMARKS, NE/N011112/1, and TONIC, NE/V01823X/1). A.P. acknowledges US-NSF funding (OCE-2100537 and 1843285). We are particularly grateful to Nina Papadomanolaki for enthusiastic discussions and sharing figure templates. A. Ralph and R. Rees-Owen are acknowledged for preparing samples; Dr S. Grimes and Dr H Manner are acknowledged for the guidance to the Zumaia Section; N. Muzylöv is acknowledged for providing samples from Guru-Fatima. E.A. Shcherbinina and Y. Gavrilov are both gratefully acknowledged for their pioneering work on the Peri-Tethyan sites that enabled this biomarker investigation and helping procure samples.

References

Anagnostou, E., John, E., Edgar, K., Foster, G.L., Ridgwell, A., Inglis, G., Pancost, R.D., Lunt, D., 2016. Changing atmospheric CO_2 concentration was the primary driver of early Cenozoic climate. *Nature* 533, 380-384

Arthur, M.A., Schlanger, S.O., Jenkyns, H.C., 1987. The Cenomanian/Turonian Oceanic Anoxic Event, II: Palaeoceanographic controls on organic matter production and preservation. Spec. Publ. Geol. Soc. London 26, 401–420.

Babila T.L. et al., 2022. Surface ocean warming and acidification driven by rapid carbon release precedes Paleocene-Eocene Thermal Maximum. *Sci. Adv* 8**,**eabg1025.

Bowen, G., Zachos, J., 2010. Rapid carbon sequestration at the termination of the

832 Palaeocene–Eocene Thermal Maximum. *Nature Geosci* 3, 866–869.
833 https://doi.org/10.1038/ngeo1014

834 Bown, P. R., 2005. Calcareous nannoplankton evolution: a tale of two oceans.
835 *Micropaleontology*, *51*, 299-308.

836 Canudo, J.I., Keller, G., Molina, E., Ortiz, N., 1995. Planktic foraminiferal turnover and $\delta^{13}C$
837 isotopes across the Paleocene-Eocene transition at Caravaca and Zumaya, Spain.
838 Palaeogeogr. Palaeoclimatol. Palaeoecol. 114, 75–100. doi:10.1016/0031-
839 0182(95)00073-U

840 Van Cappellen, P., Ingall, E. D., 1996. Redox stabilization of the atmosphere and oceans by
841 phosphorus-limited marine productivity. *Science* 271, 493-496.

842 Carmichael, M.J., Inglis, G.N., Badger, M.P.S., Naafs, B.D.A., Behrooz, L., Remmelzwaal,
843 S., Monteiro, F.M., Rohrssen, M., Farnsworth, A., Buss, H.L., Dickson, A.J., Valdes,
844 P.J., Lunt, D.J., Pancost, R.D., 2017. Hydrological and associated biogeochemical
845 consequences of rapid global warming during the Paleocene-Eocene Thermal
846 Maximum. *Glob. Planet. Change* 157, 114–138. doi:10.1016/j.gloplacha.2017.07.014

847 Clarkson, M.O., Lenton, T.M., Andersen, M.B. *et al.,* 2021. Upper limits on the extent of
848 seafloor anoxia during the PETM from uranium isotopes. *Nat Commun* 12, 399.
849 https://doi.org/10.1038/s41467-020-20486-5.

850 Dickens, G.R., Castillo, M.M., Walker, J.C.G., 1997. A blast of gas in the latest Paleocene:
851 Simulating first-order effects of massive dissociation of oceanic methane hydrate.
852 *Geology* 25, 259–262.

853 Dickson, A.J., Cohen, A.S., Coe, A.L., 2012. Seawater oxygenation during the Paleocene-
854 Eocene Thermal Maximum. *Geology* 40, 639–642. doi:10.1130/G32977.1

855 Dickson, A.J., Cohen, A.S., Coe, A.L., 2014a. Continental margin molybdenum isotope
856 signatures from the early Eocene. *Earth Planet. Sci. Lett.* 404, 389–395.
857 doi:10.1016/j.epsl.2014.08.004

858 Dickson, A.J., Rees-Owen, R.L., März, C., Coe, A.L., Cohen, A.S., Pancost, R.D., Taylor, K.,
859 Shcherbinina, E., 2014b. The spread of marine anoxia on the northern Tethys margin
860 during the Paleocene-Eocene Thermal Maximum. *Paleoceanography* 29, 471–488.
861 doi:10.1002/2014PA002629

862 Dickson, A. J., 2017. A molybdenum-isotope perspective on Phanerozoic deoxygenation
863 events. *Nat. Geosci.* 10, 721–726.

Duller, R.A., Armitage, J.J., Manners, H.R., Grimes, S., Jones, T.D., 2019. Delayed sedimentary response to abrupt climate change at the Paleocene-Eocene boundary, northern Spain. *Geology* 47, 159–162. doi:10.1130/G45631.1

Dunkley Jones, T., Ridgwell, A., Lunt, D. J., Maslin, M. A., Schmidt, D. N., Valdes, P. J., 2010. Palaeogene perspective on climate sensitivity and methane hydrate instability. *Phil. Trans. R. Soc. A.* 368, 2395–2415. http://doi.org/10.1098/rsta.2010.0053

Dunkley Jones, T., Manners, H.R., Hoggett, M., Turner, S.K., Westerhold, T., Leng, M.J., Pancost, R.D., Ridgwell, A., Alegret, L., Duller, R., Grimes, S.T., 2018. Dynamics of sediment flux to a bathyal continental margin section through the Paleocene-Eocene Thermal Maximum. Clim. Past 14, 1035–1049.

Elling, F.J., Gottschalk, J., Doeana, K.D., Kusch, S., Hurley, S.J., Pearson, A, 2019. Archaeal lipid biomarker constraints on the Paleocene-Eocene carbon isotope excursion. *Nat Commun*. 10, 4519

Farrington, J.W., Davis, A.C., Sulanowski, J., McCaffrey, M.A., McCarthy, M., Clifford, C.H., Dickinson, P., Volkman, J.K., 1988. Biogeochemistry of lipids in surface sediments of the Peru Upwelling Area at 15°S. *Org. Geochem.* 13, 607–617. doi:10.1016/0146-6380(88)90080-0

Friedrich, O., 2010. Benthic foraminifera and their role to decipher paleoenvironment during mid-Cretaceous Oceanic Anoxic Events – the “anoxic benthic foraminifera” paradox. *Rev. Micropaléontologie* 53, 175–192. doi:10.1016/j.revmic.2009.06.001

Frieling, J., Gebhardt, H., Huber, M., Adekeye, O.A., Akande, S.O., Reichart, G.J., Middelburg, J.J., Schouten, S., Sluijs, A., 2017. Extreme warmth and heat-stressed plankton in the tropics during the Paleocene-Eocene Thermal Maximum. *Sci. Adv.* 3, e1600891. doi:10.1126/sciadv.1600891

Frieling, J., Iakovleva, A.I., Reichart, G.-J., Aleksandrova, G.N., Gnibidenko, Z.N., Schouten, S., Sluijs, A., 2014. Paleocene-Eocene warming and biotic response in the epicontinental West Siberian Sea. *Geology* 42, 767–770. doi:10.1130/G35724.1

Frieling, J., Peterse, F., Lunt, D. J., Bohaty, S. M., Sinninghe Damsté, J. S., Reichart, G. J., & Sluijs, A., 2019. Widespread warming before and elevated barium burial during the Paleocene-Eocene Thermal Maximum: Evidence for methane hydrate release? *Paleoceanography and Paleoclimatology* 34, 546– 566.

Gavrilov, Y.., Shcherbinina, E.A., Oberhansli Hedi, 2003. Paleocene-Eocene boundry events

in the northeastern Peri-Tethys, in: Wing, S.L., Gingerich, P.D., Schmitz, B., Thomas, E. (Eds.), Causes and Consequences of Globally Warm Climates in the Early Paleogene. Geological Society of America Special Paper 369, Boulder, Colorado.

Gavrilov, Y., Shcherbinina, E., Golovanova, O., Pokrovsky, B., 2009. A variety of PETM records in different setting, northeastern Peri-Tethys. *Clim. Biotic Events Paleogene* 1–4.

Goddéris, Y., Donnadieu, Y., Le Hir, G., Lefebvre, V., Nardin, E., 2014. The role of palaeogeography in the Phanerozoic history of atmospheric CO_2 and climate. *Earth-Science Rev*. doi:10.1016/j.earscirev.2013.11.004

Gutjahr, M., Ridgwell, A., Sexton, P. *et al.*, 2017. Very large release of mostly volcanic carbon during the Palaeocene–Eocene Thermal Maximum. *Nature* 548, 573–577.

Handley, L., O'Halloran, A., Hawkins, E., Nicholas, C.J., Pearson, P.N., McMillan, I.K., and Pancost, R.D., 2012. Increases in terrestrial runoff and seasonal precipitation but enhanced aridity during the Paleocene-Eocene Thermal Maximum in Tanzania. *Palaeogeoghaphy, Palaeoclimatology, Palaeoecology* 329, 10-21.

Hess, A.V., Auderset, A., Rosenthal, Y. *et al.*, 2023. A well-oxygenated eastern tropical Pacific during the warm Miocene. *Nature* 619, 521–525. https://doi.org/10.1038/s41586-023-06104-6

Hayes, J.M., Freeman, K.H., Popp, B.N., Hoham, C.H. (1990) Compound-specific isotopic analyses: A novel tool for reconstruction of ancient biogeochemical processes. *Org. Geochem.* 16, 1115–1128.

Hayes, J.M., 1993. Factors controlling ^{13}C contents of sedimentary organic compounds: Principles and evidence. *Mar. Geol.* 113, 111–125.

Higgins, M.B., Robinson, R.S., Husson, J.M., Carter, S.J., Pearson, A., 2012. Dominant eukaryotic export production during ocean anoxic events reflects the importance of recycled NH_4^+. *Proceedings of the National Academy of Sciences of the United States of America* 109, 2269-2274.

Inglis, G.N., Bragg, F., Burls, N., Evans, D., Foster, G., Huber, M., Lunt, D., Siler, N., Steinig, S., Wilkinson, R., Anagnostou, E., Cramwinckel, M., Hollis, C., Pancost, R., Tierney, J.E., 2020. Global mean surface temperature and climate sensitivity of the EECO, PETM and latest Paleocene. *Clim. Past Discuss*. 44, 1–43. doi:10.31223/OSF.IO/8527Z

928 Jenkyns, H.C., 2010. Geochemistry of oceanic anoxic events. G*eochemistry, Geophys.*
929 *Geosystems* 11, Q03004. doi:10.1029/2009GC002788

930 John, C. M., Bohaty, S.M., Zachos, J.C., Sluijs, A., Gibbs, S., Brinkhuis, H., Bralower, T.J.,
931 2008. North American continental margin records of the Paleocene-Eocene thermal
932 maximum: Implications for global carbon and hydrological cycling, Paleoceanography,
933 23, PA2217, doi:10.1029/2007PA001465.

934 Junium, C.K., Arthur, M.A., 2007. Nitrogen cycling during the Cretaceous, Cenomanian-
935 Turonian Oceanic Anoxic Event II. *Geochemistry, Geophysics, Geosystems* 8,
936 Q03002. doi: 10.1029/2006GC001328

937 Junium, C.K., Dickson, A.J., Uveges, B.T., 2018. Perturbation to the nitrogen cycle during
938 rapid Early Eocene global warming. *Nat. Commun.* 9, 3186. doi:10.1038/s41467-018-
939 05486-w

940 Kennett, J.P., Stott, L.D., 1991. Abrupt deep-sea warming, palaeoceanographic changes
941 and benthic extinctions at the end of the Palaeocene. *Nature* 353, 225–229.
942 doi:10.1038/353225a0

943 Knies J., Mann U., Popp B.N., Stein R., 2008. Surface water productivity and
944 paleoceanographic implications in the Cenozoic Arctic Ocean. *Paleoceanography* 23,
945 1–12. doi: 10.1029/2007PA001455

946 Koopmans, M.P., Köster, J., Van Kaam-Peters, H.M.E.E., Kenig, F., Schouten, S., Hartgers,
947 W.A., De Leeuw, J.W., Sinninghe Damsté, J.S., 1996. Diagenetic and catagenetic
948 products of isorenieratene: Molecular indicators for photic zone anoxia. *Geochim.*
949 *Cosmochim. Acta* 60, 4467–4496. doi:10.1016/S0016-7037(96)00238-4

950 Kuypers, M.M.M., Pancost, R.D., Nijenhuis, I.A., Sinninghe Damsté, J.S., 2002. Enhanced
951 productivity led to increased organic carbon burial in the exinic North Atlantic basin
952 during the late Cenomanian oceanic anoxic event. *Paleoceanography* 17, 1051.
953 doi:10.1029/2000PA000569

954 Li, M.W., Larter, S.R., Taylor, P., Jones, D.M., Bowler, B., Bjorøy, M., 1995. Biomarkers or
955 not biomarkers? A new hypothesis for the origin of pristane involving derivation from
956 methyltrimethyltridecylchromans (MTTCs) formed during diagenesis from chlorophyll
957 and alkylphenols. *Org. Geochem*. 23, 159-167

958 Lyons, S.L., Baczynski, A.A., Babila, T.L. *et al.* Palaeocene–Eocene Thermal Maximum
959 prolonged by fossil carbon oxidation. *Nature Geosci* **12**, 54–60 (2019).

960 Mackenzie, A.S., Patience, R.L., Maxwell, J.R., Vandenbroucke, M., Durand, B., 1980.
961 Molecular parameters of maturation in the Toarcian shales, Paris Basin, France—I.
962 Changes in the configurations of acyclic isoprenoid alkanes, steranes and triterpanes.
963 *Geochim. Cosmochim. Acta* 44, 1709–1721. doi:10.1016/0016-7037(80)90222-7

964 Manners, H.R., Grimes, S.T., Sutton, P.A., Domingo, L., Leng, M.J., Twitchett, R.J., Hart,
965 M.B., Dunkley Jones, T., Pancost, R.D., Duller, R., Lopez-Martinez, N., 2013.
966 Magnitude and profile of organic carbon isotope records from the Paleocene-Eocene
967 Thermal Maximum: Evidence from northern Spain. *Earth Planet. Sci. Lett.* 376, 220–
968 230. doi:10.1016/j.epsl.2013.06.016

969 Miller, K. G., Wright, J. D. & Fairbanks, R. G., 1991. Unlocking the ice house: Oligocene-
970 Miocene oxygen isotopes, eustasy, and margin erosion. *J. Geophys. Res. Solid*
971 *Earth* 96, 6829–6848.

972 Molina, E., Appenillas, I., Pardo, A., 1999. High resolution planktic foraminiferal
973 biostratigraphy and correlation across the Paleocene/Eocene boundary in the Tethys.
974 *Bull. la Socie´te´ Ge´ologique Fr.* 170, 521–530.

975 Monteiro, F.M., Pancost, R.D., Ridgwell, A., Donnadieu, Y., 2012. Nutrients as the dominant
976 control on the spread of anoxia and euxinia across the Cenomanian-Turonian oceanic
977 anoxic event (OAE2): Model-data comparison. *Paleoceanography* 27, 1–17.
978 doi:10.1029/2012PA002351

979 Naafs, B.D.A. & Pancost, R.D., 2014. Environmental conditions in the South Atlantic (Angola
980 Basin) during the Early Cretaceous. *Organic Geochemistry* 76, 184-193.
981 10.1016/j.orggeochem.2014.08.005.

982 Naafs, B.D.A., Monteiro, F.M., Pearson, A., Higgins, M.B., Pancost, R.D., Ridgwell, A., 2019.
983 Fundamentally different global marine nitrogen cycling in response to severe ocean
984 deoxygenation. *Proc. Natl. Acad. Sci.* 116, 24979–24984.
985 doi:10.1073/pnas.1905553116

986 O'Brien, C.L., Robinson, S.A., Pancost, R.D., Sinninghe, J.S., Schouten, S., Lunt, D.J.,
987 Alsenz, H., Bornemann, A., Bottini, C., Brassell, S.C., Farnsworth, A., Forster, A.,
988 Huber, B.T., Inglis, G.N., Jenkyns, H.C., Linnert, C., Littler, K., Markwick, P., Mcanena,
989 A., Mutterlose, J., Naafs, B.D.A., Püttmann, W., Sluijs, A., Helmond, N.A.G.M. Van,
990 Vellekoop, J., Wagner, T., Wrobel, N.E., 2017. Earth-Science Reviews Cretaceous
991 sea-surface temperature evolution : Constraints from TEX_{86} and planktonic
992 foraminiferal oxygen isotopes. *Earth-Science Rev*. 172, 224–247.
993 doi:10.1016/j.earscirev.2017.07.012

994 Overmann, J., 2008. In *Sulfur Metabolism in Phototrophic Organisms* Vol. 27 *Advances in*
995 *Photosynthesis and Respiration* (Eds Rüdiger Hell *et al.*) Springer Netherlands; pp.
996 375-396.

997 Owens, J. D., Reinhard, C.T., Rohrssen, M., Love, G.D., Lyons, T.W., 2016. Empirical links
998 between trace metal cycling and marine microbial ecology during a large perturbation
999 to Earth's carbon cycle. *Earth and Planetary Science Letters* 449, 407-417.
1000 https://doi.org/10.1016/j.epsl.2016.05.046

1001 Pagani, M., Pedentchouk, N., Huber, M. *et al.*, 2006. Arctic hydrology during global warming
1002 at the Palaeocene/Eocene thermal maximum. *Nature* 442, 671–675.

1003 Pancost, R. D., Hopmans, E. C., Sinninghe Damsté, J. S., and the MEDINAUT Shipboard
1004 Scientific Party, 2001. Archaeal lipids in Mediterranean cold seeps: Molecular proxies
1005 for anaerobic methane oxidation. *Geochimica Cosmochimica Acta* 65, 1611-1627.

1006 Pancost, R.D., Crawford, N., Magness, S., Turner, A., Jenkyns, H.C., Maxwell, J.R., 2004.
1007 Further evidence for the development of photic-zone euxinic conditions during
1008 Mesozoic oceanic anoxic events. *J. Geol. Soc. London.* 161, 353–364.
1009 doi:10.1144/0016764903-059

1010 Papadomanolaki, N. M., Sluijs, A. & Slomp, C. P., 2022. Eutrophication and Deoxygenation
1011 Forcing of Marginal Marine Organic Carbon Burial During the PETM.
1012 *Paleoceanography and Paleoclimatology* 37, e2021PA004232.

1013 Pogge von Strandmann, P.A.E., Jenkyns, H. & Woodfine, R., 2013. Lithium isotope evidence
1014 for enhanced weathering during Oceanic Anoxic Event 2. *Nature Geosci* 6, 668–672.

1015 Pogge von Strandmann, P.A.E., Jones, M.T., West, A.J., Murphy, M.J., Stokke, E.W.,
1016 Tarbuck, G., Wilson, D.J., Pearce, C.R., Schmidt, D.N., 2021. Lithium isotope
1017 evidence for enhanced weathering and erosion during the Paleocene-Eocene Thermal
1018 Maximum. *Science Advances* 7, eabh4224.

1019 Pujalte, V., Baceta, J.I., Orue-Etxebarria, X., Payros, A., 1998. Paleocene Strata Of The
1020 Basque Country, Western Pyrenees, Northern Spain: Facies and sequence
1021 development in a deep-water starved basin. *Mesozoic Cenozoic Seq. Stratigr. Eur.*
1022 *Basins* 60, 311–325. doi:10.2110/pec.98.02.0303

1023 Rattanasriampaipong, R, Zhang, Y.G., Pearson, A., Hedlund, B.P., Zhang, S., 2022.
1024 Archaeal lipids trace ecology and evolution of marine ammonia-oxidizing archaea.

Proc Natl Acad Sci U S A 119:e2123193119.

Remmelzwaal, S.R.C., Dixon, S., Parkinson, I.J., Schmidt, D.N., Monteiro, F.M., Sexton, P., Fehr, M.A., Peacock, C., Donnadieu, Y., James, R.H., 2019. Investigating ocean deoxygenation during the PETM through the Cr isotopic signature of foraminifera. *Paleoceanogr. Paleoclimatology* 917–929. doi:10.1029/2018pa003372

Ridgwell, A., Hargreaves, J.C., Edwards, N.R., Annan, J.D., Lenton, T.M., Marsh, R., Yool, A., Watson, A., 2007. Marine geochemical data assimilation in an efficient Earth System Model of global biogeochemical cycling. *Biogeosciences Discuss.* 4, 87–104.

Rodríguez-Tovar, F.J., Uchman, A., Alegret, L., Molina, E., 2011. Impact of the Paleocene–Eocene Thermal Maximum on the macrobenthic community: Ichnological record from the Zumaia section, northern Spain. *Mar. Geol.* 282, 178–187. doi:10.1016/j.margeo.2011.02.009

Robinson, S. A., Heimhofer, U., Hesselbo, S. P. & Petrizzo, M. R., 2017. Mesozoic climates and oceans – a tribute to Hugh Jenkyns and Helmut Weissert. *Sedimentology* 64, 1-15, (2017).

Robinson, S. A., Dickson, A. J., Pain, A., Jenkyns, H. C., O'Brien, C. L., Farnsworth, A. & Lunt, D. J., 2019. Southern Hemisphere sea-surface temperatures during the Cenomanian–Turonian: Implications for the termination of Oceanic Anoxic Event 2. *Geology* 47, 131-134.

Schlanger, S.O., Jenkyns, H.C., S. O. Schlanger, H.C.J., Schlanger, S.O., Jenkyns, H.C., 1976. Cretaceous Oceanic Anoxic Events: Causes and Concequences. *Geol. En Minbouw* 55, 179–184.

Schoon, P.L., Heilmann-Clausen, C., Schultz, B.P., Sluijs, A., Sinninghe Damsté, J.S., Schouten, S., 2013. Recognition of Early Eocene global carbon isotope excursions using lipids of marine Thaumarchaeota. *Earth Planet. Sci. Lett.* 373, 160–168. doi:10.1016/j.epsl.2013.04.037

Schoon, P. L., Heilmann-Clausen, C., Schultz, B.P., Sinninghe Damsté, J. S., & Schouten, S., 2015. Warming and environmental changes in the eastern North Sea Basin during the Palaeocene–Eocene Thermal Maximum as revealed by biomarker lipids. *Organic Geochemstry*, 78, 79–88.

Schouten, S.., Hopmans, E. C., Schefuss, E. & Sinninghe Damsté, J. S., 2002. Distributional variations in marine crenarchaeotal membrane lipids: a new tool for reconstructing ancient sea water temperatures? *Earth Planet. Sci. Lett.* 204, 265-274.

1058 Schouten, S., Hopmans, E.C., Sinninghe Damsté, J.S., 2004. The effect of maturity and
1059 depositional redox conditions on archaeal tetraether lipid palaeothermometry. *Organic*
1060 *Geochemistry* 35, 567-571.

1061 Schouten, S., Hopmans, E.C., Sinninghe Damsté, J.S., 2013. The organic geochemistry of
1062 glycerol dialkyl glycerol tetraether lipids: A review. *Organic Geochemistry* 54, 19-61.

1063 Schulte, S., Rostek, F., Bard, E., Rullkötter, J., Marchal, O., 1999. Variations of oxygen-
1064 minimum and primary productivity recorded in sediments of the Arabian Sea. *Earth*
1065 *Planet. Sci. Lett.* 173, 205–221. doi:10.1016/S0012-821X(99)00232-0

1066 Shcherbinina, E., Gavrilov, Yu., Iakovleva, A., Pokrovsky, B., Golovanova, O., and
1067 Aleksandrova, G., 2016. Environmental dynamics during the Paleocene-Eocene
1068 thermal maximum (PETM) in the northeastern Peri-Tethys revealed by high resolution
1069 micropalaeontological and geochemical studies of a Caucasian key
1070 section, *Palaeogeogr., Palaeoclimatol., Palaeoecol*. 456, 60–81.

1071 Sinninghe Damsté, J. S. & Köster, J. A., 1998. A euxinic southern North Atlantic Ocean
1072 during the Cenomanian/Turonian oceanic anoxic event. *Earth Planet. Sci. Lett.* 158,
1073 165-173.

1074 Sinninghe Damsté, J.S., Kuypers, M.M.M., Schouten, S., Schulte, S., Rullkötter, J., 2003.
1075 The lycopane/C_{31} *n*-alkane ratio as a proxy to assess palaeoxicity during sediment
1076 deposition. *Earth Planet. Sci. Lett.* 209, 215–226. doi:10.1016/S0012-821X(03)00066-
1077 9

1078 Sluijs, A., Schouten, S., Pagani, M., Woltering, M., Brinkhuis, H., Damsté, J.S.S., Dickens,
1079 G.R., Huber, M., Reichart, G.-J., Stein, R., Matthiessen, J., Lourens, L.J.,
1080 Pedentchouk, N., Backman, J., Moran, K., the Expedition 302 Scientists, 2006.
1081 Subtropical Arctic Ocean temperatures during the Palaeocene/Eocene thermal
1082 maximum. *Nature* 441, 610–613. doi:10.1038/nature04668

1083 Sluijs, A., Brinkhuis, H., Crouch, E.M., John, C.M., Handley, L., Munsterman, D., Bohaty,
1084 S.M., Zachos, J.C., Reichart, G.-J., Schouten, S., Pancost, R.D., Sinninghe
1085 Damsté, J.S., Welters, N.L.D., Lotter, A.F., Dickens, G.R., 2008. Eustatic variations
1086 during the Paleocene-Eocene greenhouse world, *Paleoceanography* 23, PA4216,
1087 doi:10.1029/2008PA001615.

1088 Sluijs, A., Bijl, P.K., Schouten, S., Röhl, U., Reichart, G.J., Brinkhuis, H., 2011. Southern
1089 Ocean warming, sea level and hydrological change during the Paleocene–Eocene
1090 thermal maximum. *Climate of the Past* 7, 47-61.

Sluijs, A., van Roij, L., Harrington, G.J., Schouten, S., Sessa, J.A., LeVay, L.J., Reichart, G.-J., Slomp, C.P., 2014. Warming, euxinia and sea level rise during the Paleocene–Eocene Thermal Maximum on the Gulf Coastal Plain: implications for ocean oxygenation and nutrient cycling. *Clim. Past* 10, 1421–1439. doi:10.5194/cp-10-1421-2014

Summons, R.E., Powell, T.G., Boreham, C.J., 1988. Petroleum geology and geochemistry of the Middle Proterozoic McArthur Basin, Northern Australia: III. Composition of extractable hydrocarbons. *Geochim. Cosmochim. Acta* 52, 1747–1763. doi:10.1016/0016-7037(88)90001-4

Svensen, H., Planke, S., Malthe-Sørenssen, A., Jamtveit, B., Myklebust, R., Rasmussen Eidem, T., Rey, S.S., Dickens, G.R., Castillo, M.M., Walker, J.C.G., Zeebe, R.E., Zachos, J.C., Dickens, G.R., 2004. Release of methane from a volcanic basin as a mechanism for initial Eocene global warming. *Nature* 429, 542.

Taylor, K.W.R., Huber, M., Hollis, C.J., Hernandez-Sanchez, M.T., Pancost, R.D., 2013. Re-evaluating modern and Paleogene GDGT distributions: Implications for SST reconstructions. *Global Planetary Change* 108, 158-174.

Taylor, L.L., Leake, J.R., Quirk, J., Hardy, K., Banwart, S.A. And Beerling, D.J., 2009. Biological weathering and the long-term carbon cycle: integrating mycorrhizal evolution and function into the current paradigm. *Geobiology* 7, 171-191.

Tierney, J.E. & Tingley, M.P. (2014) A Bayesian, spatially-varying calibration model for the TEX_{86} proxy. *Geochimica et Cosmochimica Acta*, 127, 83-106. https://doi.org/10.1016/j.gca.2013.11.026.

Trabucho-Alexandre, J., Dirkx, R., Veld, H., Klaver, G., de Boer, P., 2012. Toarcian Black Shales in the Dutch Central Graben: Record of energetic, variable depositional conditions during an Oceanic Anoxic Event. *Journal of Sedimentary Research* 82. 104-120. 10.2110/jsr.2012.5.

Volkman, J.K., Maxwell, J.R., 1986. Acyclic isoprenoids as biological markers. In (R.B. Johns, Ed.) *Biological Markers in the Sedimentary Record*, Elsevier, Amsterdam, pp. 1-46

Wagner, T., Sinninghe Damsté, J.S., Hofmann, P., Beckmann, B., 2004. Euxinia and primary production in Late Cretaceous eastern equatorial Atlantic surface waters fostered orbitally driven formation of marine black shales. *Paleoceanography* 19, 1–13.

Weijers, J.W.H., Schouten, S., Spaargaren, O.C., Sinninghe Damsté, J.S., 2006. Occurrence and distribution of tetraether membrane in soils: implications for the use of the BIT index and the TEX_{86} SST proxy. *Org Geochem.* 37, 1680-1693.

Westerhold, T., Röhl, U., Wilkens, R.H., Gingerich, P.D., Clyde, W.C., Wing, S.L., Bowen, G.J., Kraus, M.J., 2018. Synchronizing early Eocene deep-sea and continental records – cyclostratigraphic age models for the Bighorn Basin Coring Project drill cores. *Clim. Past* 14, 303–319. doi:10.5194/cp-14-303-2018

Winguth, A.M.E., Thomas, E., Winguth, C., 2012. Global decline in ocean ventilation, oxygenation and productivity during the Paleocene-Eocene Thermal Maximum – Implications for the benthic extinction. *Geology*, 40, 263-266.

Witkowski, C.R., Weijers, J.W.H., Blais, B., Schouten, S., Sinninghe Damsté, J.S., 2018. Molecular fossils from phytoplankton reveal secular Pco_2 trend over the Phanerozoic. *Sci. Adv.* 4, eaat4556.

Yao, W., Paytan, A., & Wortmann, U. G. (2018). Large-scale ocean deoxygenation during the Paleocene-Eocene thermal maximum. *Science*, 361, 804– 806.

Zachos, J.C., Schouten, S., Bohaty, S., Quattlebaum, T., Sluijs, A., Brinkhuis, H., Gibbs, S.J., Bralower, T.J., 2006. Extreme warming of mid-latitude coastal ocean during the Paleocene-Eocene Thermal Maximum: Inferences from TEX_{86} and isotope data. *Geology* 34, 737–740. doi:10.1130/G22522.1

Zeebe, R.E., Zachos, J.C., Dickens, G.R., 2009. Carbon dioxide forcing alone insufficient to explain Palaeocene–Eocene Thermal Maximum warming. *Nat. Geosci.* 2, 576–580.

Zhou, X., Thomas, E., Rickaby, R. E. M., Winguth, A. M. E., and Lu, Z., 2014. I/Ca evidence for upper ocean deoxygenation during the PETM, *Paleoceanography*, 29, 964– 975.